Stressed Micromachined Magnetic Actuators for Micro-mirror Applications

Jeremy T.M.G. Johnson

Department of Electrical and Computer Engineering
University of Manitoba
Winnipeg, Manitoba, Canada

A thesis submitted to
the Faculty of Graduate Studies
in partial fulfillment of
the requirements for the degree of

Master of Science

THE UNIVERSITY OF MANITOBA

FACULTY OF GRADUATE STUDIES

*****

COPYRIGHT PERMISSION

Stressed Micromachined Magnetic Actuators for Micro-mirror Applications

BY

Jeremy T.M.G. Johnson

A Thesis/Practicum submitted to the Faculty of Graduate Studies of The University of Manitoba in partial fulfillment of the requirement of the degree

OF

Master of Science

To my late grandfather,

ABSTRACT

This paper discusses the development of an out-of-plane micromachined magnetic actuator for micro-mirror applications. Lorentz forces are used to actuate the microstructures that are fabricated to have an initial out-of-plane rest angle. Magnetic microelectromechanical systems (MEMS) have the advantage of large actuation distances with low power requirements. An inexpensive fabrication process is developed using aluminum and chrome thin films for a device layer, and a silicon sacrificial. A photoresist sacrificial layer is also attempted with limited fabrication success due to problems with photoresist residues and device release. Several different device designs are attempted to determine a suitable design for the fabrication process. This design is also implemented in a micro-mirror array to observe variability in the fabrication of the structures as well as the consistency in actuation. The resonant frequency and lifetime of the micro-mirror structures are also examined. A model is developed in order to predict the actuation of the micro-mirror devices.

ACKNOWLEDGEMENTS

I would like to thank my advisor, Dr. Cyrus Shafai, for all his support and assistance throughout this project. His knowledge in the many aspects of the project were much appreciated.

I would also like to thank my colleagues, Kwan-yu Lai, Joe Yip, Alfred Lip and Karmun Cheng for keeping me sane through this long and difficult journey.

I also thank the many technicians, professors and assistants for helping in the construction and maintenance of the microfabrication lab. I would especially like to thank Allan McKay, Doug Buchanan, and Lianne Lester.

I would like to thank my parents who have always shown me support throughout both my academic and non-academic life. Without their encouragement, none of this would have been possible. Thanks also to the rest of my friends and family for always being there for me when I need them the most. I would like to give special thanks to the late Morley Greenham and Emil Johnson, who have both taught me so much about life.

Thanks also to the National Science and Engineering Research Council of Canada (NSERC) and Novra Technologies Incorporated for helping fund this project.

TABLE OF CONTENTS

ABSTRACT ..... **I**

ACKNOWLEDGEMENTS ..... **II**

TABLE OF CONTENTS ..... **III**

LIST OF FIGURES ..... **V**

LIST OF TABLES ..... **VII**

LIST OF SYMBOLS ..... **VIII**

ABBREVIATIONS ..... **IX**

1. INTRODUCTION **1**

1.1 Motivation 1
1.2 Organization of Thesis 2

2. MICROFABRICATION AND MEMS **4**

2.1 Microelectomechanical Systems 4
2.1.1 Magnetic MEMS 6
2.2 Microfabrication Techniques 7
2.2.1 Lithography 8
2.2.2 Thermal Evaporation 10
2.2.3 Sputtering 12
2.2.4 Wet Chemical Etching 14
2.2.5 Plasma Etching 16
2.2.6 Xenon Difluoride Etching 17
2.2.7 Sacrificial Materials 19
2.3 Micro-mirrors 22
2.3.1 Texas Instruments Digital Light Processing (DLP) Mirror 22
2.3.2 Seoul National University Micro-mirror 23
2.3.3 Electrostatic/Magnetic Latching Micro-mirrors 25
2.3.4 Lucent LambdaRouter 28
2.4 Single Loop Lorentz Force Actuators 29
2.5 Lorentz Force Micro-mirrors 31
2.5.1 2-D Lorentz Force Actuated Micro-mirrors 31
2.5.2 Laterally Driven Electromagnetic Microactuators 32
2.6 Thin Film Stress 34

3. DESIGN AND MODELLING OF MAGNETIC MICRO-MIRRORS **38**

3.1 Design concept 38
3.2 Actuation Mechanisms 40
3.2.1 Material Properties 41
3.2.2 Thermal Expansion 41
3.2.3 Lorentz (Magnetic) Forces 48
3.2.4 Electrostatic Forces 50
3.3 Force Comparison 51
3.3.1 Electrostatic and Magnetic Force Comparison 51
3.3.2 Thermal and Magnetic Force Comparison 55

4. FABRICATION OF MAGNETIC MICRO-MIRROR STRUCTURES **57**

4.1 Patterned and Unpatterned Sacrificial Designs 57
4.2 Fabrication with a Photoresist Sacrificial 59
4.2.1 Photoresist Sacrificial Method with Acetone Release 60
4.2.2 Photoresist Sacrificial Method with Post-Release Processing 62

4.2.3 Photoresist Sacrificial Method with Plasma Release 64
4.2.4 Sidewall Issues with Photoresist Sacrificial 67
4.3 Fabrication with Silicon Sacrificial 68
4.3.1 Patterned Silicon Sacrificial Method using DC Sputtering 68
4.3.2 Unpatterned Silicon Sacrificial Method using DC Sputtering 70
4.3.3 Unpatterned Silicon Sacrificial Method using RF Sputtering 72

5. FABRICATION ANALYSIS OF STRESSED MAGNETIC MICRO-MIRRORS 75

5.1 Silicon Sacrificial Gas Loading Problem with XeF_2 76
5.2 Silicon Sacrificial Residues 76
5.3 Chrome Length and Rest Angle 79
5.4 Fabrication Consistency 81
5.4.1 Fabrication Consistency Design 82
5.4.2 Fabrication Process of Micro-mirror Arrays 83
5.4.3 Design Compatibility with Fabrication 84
5.4.4 Initial Rest Angle Variation 85
5.5 Issues with an Unpatterned Silicon Sacrificial Layer 88

6.TESTING AND MODEL VERIFICATION OF MAGNETIC MICRO-MIRRORS 90

6.1 Current Driven Failure 91
6.2 Transition Angle 92
6.3 Thermal Response 92
6.4 Magnetic Response 94
6.4.1 Deflection Range 95
6.4.2 Different Geometries 96
6.5 Model Verification of Magnetic Micro-mirror 99
6.6 Frequency Testing 101
6.7 Micromirror Lifetime 104

7. CONCLUSION 105

7.1 Summary 105
7.2 Future Work and Recommendations 105

BIBLIOGRAPHY 107

APPENDICIES 110

APPENDIX A. Flowchart of XeF_2 Quick Pulse Etching 110
APPENDIX B. Mask Layouts 111
APPENDIX C. SELF ASSEMBLY 112
C.1 Self Assembly MEMS 112
C.2 Design of Magnetic Self-Assembly Actuators 114
C.3 Magnetic Self-Assembly Results 115
APPENDIX D. MATLAB Plot code 118

LIST OF FIGURES

Figure 2-1. Karl Suss MA3 Mask Aligner in Operation 10
Figure 2-2. Examples of Bad and Good sidewall coverage 11
Figure 2-3. Schematic of a Thermal Evaporator System 12
Figure 2-4. Sputtering at the University of Manitoba's Nano-system Fabrication Laboratory (NSFL) 13
Figure 2-5. An example of underetching that occurs with wet etching (left). A wet etch performed in the microfabrication lab at the NFSL (right). 15
Figure 2-6. Plasma Etcher at the University of Manitoba's NSFL Cleanroom 16
Figure 2-7. Schematic of XeF_2 System used in this project 19
Figure 2-8. Photoresist patterning process flow 20
Figure 2-9. Schematic pixel and array of Texas Instrument's DLP System 23
Figure 2-10. Schematic of Electromagnetic Micromirror 24
Figure 2-11. Layout of magnetically actuated optical switch 26
Figure 2-12. Switching sequence of magnetically actuated optical switch 27
Figure 2-13. Lucent LambdaRouter Micromirror 28
Figure 2-14. Schematic of Self-Assembly Single Loop Lorentz Force Actuators 30
Figure 2-15. Schematic of moveable micro-grid using Single Loop Lorentz Force Actuators 30
Figure 2-16. Schematic of 2-D bridge Micromirror 32
Figure 2-17. Micro-switches using Laterally Drive Electromagnetic Microactuators 33
Figure 2-18. Microwave switch fabricated with aluminum stressed with chrome 35
Figure 3-1. A simple schematic of the proposed magnetic microactuator 39
Figure 3-2. Schematic of Thermal Heating 45
Figure 3-3. Electrostatic and Magnetic force comparison 54
Figure 3-4. Thermal and Magnetic Force Comparison 56
Figure 4-1. Cross-section fabrication process flow 58
Figure 4-3. Bubbling aluminum due to outgassing of photoresist sacrificial 61
Figure 4-4. Photoresist cracking when hard-bake time was increased to one hour 63
Figure 4-6. Severed beam structure showing photoresist residue 67
Figure 4-7. Poor Sidewall Coverage of Patterned Silicon Sacrificial 69
Figure 4-7. DC Sputtered Silicon sacrificial devices before release 71
Figure 4-8. DC Sputtered silicon sacrificial after release 72
Figure 4-9. RF Sputtered silicon sacrificial micro-mirrors before release 73
Figure 4-10. RF Sputtered silicon sacrificial micro-mirrors after release 74
Figure 5-1. Probe station in the Nanosystems Test Lab at the University of Manitoba 75
Figure 5-2. Residue present where not covered by aluminum 77
Figure 5-3. Unanchored aluminum test beams on silicon sacrifical which do not release without chrome (left), and which release when coated with chrome (right) 78
Figure 5-4. Rest angle schematic 79
Figure 5-5. Micromirror positioned at 90° to observe curvature in flexure arms 80
Figure 5-6. Angular Deflection due to Initial Stress (300x280μm reflector) 81
Figure 5-7. Schematics of four magnetic microactuators composed of aluminum (silver) and chrome (brown) 82
Figure 5-8. Examples of 4 micro-reflector array designs after release 84
Figure 5-9. Example of Initial Rest Height variation of two micro-mirror arrays 86
Figure 5-10. Three Points Measured to Determine Thickness Variation on Wafer 87
Figure 5-11. Unpatterned sacrificial etching causing variability in initial rest angle 88
Figure 6-1. Schematic of micro-mirrors under test 90

Figure 6-2. Thermal testing of micro-mirrors at 0mA (a) and 75mA (b) which deflected approximately 5mA 93
Figure 6-3. Simulation showing the projected angular deflection due to thermal heating 94
Figure 6-4. Magnetic Actuation of 800μm x 600μm micro-mirror 96
Figure 6-5. Angular deflection versus Current of Micro-mirrors with different geometry 98
Figure 6-6. Measured and Theoretical angular displacement of three fabricated designs 100
Figure 6-8. Measured Frequency Response of Magnetic Micro-mirrors using MRD500 Photodiode 103
Figure A.1 XeF_2 Quick Pulse Etching Flowchart 110
Figure B-1. Initial Stressed Magnetic Microactuator Wafer 111
Figure B-2. Micro-reflector array and Self-Assembly wafer 111
Figure C-1. Plastic Deformation Magnetic Assembly schematic [34] 113
Figure C-2. Schematic of magnetic self-assembly actuators 114
Figure C-3 Dissimilar actuation of magnetic self-assembly structures 116
Figure C-4. Poor latching of stressed magnetic actuators 117

LIST OF TABLES

Table 2-1. Chemical composition of Chrome and Aluminum Etches 15
Table 3-1. Geometric Design Parameters of the Stressed Magnetic Actuators 40
Table 3-2. Bulk Material Properties of Aluminum and Chrome 41
Table 4-1. Photoresist Sacrificial Process Parameters with acetone release 60
Table 4-2. Photoresist Sacrificial Process Parameters with post-release processing 62
Table 4-3. Photoresist Sacrificial Process Parameters with plasma release 64
Table 4-4. Sacrificial Photoresist Release Plasma etch parameters 65
Table 4-5. Patterned Silicon Sacrificial Process Parameters 69
Table 4-6. Initial Silicon Sacrificial Process Parameters 70
Table 4-7. Unpatterned Silicon Sacrificial Process Parameters using RF Sputtering 72
Table 5-1. Specifications of devices used in Rest Angle Measurements 80
Table 5-2. Geometric Design Parameters of the Stressed Magnetic Actuators 83
Table 5-3. Average and Maximum Initial Rest Angles of 4 micro-mirror arrays 85
Table 5-4. Film Thickness Variation over the Wafer Surface 86
Table 6-1. Design Parameters of the Actuated Micro-mirrors 90
Table 6-2. Maximum and Minimum Currents before flexure failure 91
Table 6-3. 800μmx600μm Magnetic Micro-mirror (800μm chrome length) with 28μm flexure and 250μm reflector 95
Table 6-4. Dimensions of the micro-mirrors under test (56μm Flexure widths, 300μm Reflector Length) 97
Table 6-5. Angular deflection vs. applied current 97

LIST OF SYMBOLS

α_T	Thermal Expansion Coefficient
ρ	Resistivity
σ_y	Yield Stress
A	Area
E_m	Young's Modulus
F	Force
I	Current
I_m	Moment of Inertia
L_A	Flexure Length
L_C	Chrome Length
L_R	Reflector Length
L_m	Length of Bending Region
M_y	Yield Moment
ΔT	Change in Temperature
t_A	Aluminum Thickness
t_C	Chrome Thickness
T	Torque
t_m	Beam Thickness
W_m	Beam Width
W_A	Flexure Width
W_R	Reflector Width

ABBREVIATIONS

CCD	Charge-coupled Device
DLP	Digital Light Processor
DPI	Dots per Inch
HF	Hydrofluoric Acid
KOH	Potassium Hydroxide
MEMS	Microelectromechanical Systems
MOEMS	Micro-optical-electromechanical Systems
O_2	Oxygen
PDMA	Plastic Deformation Magnetic Assembly
RPM	Rotations Per Minute
SiO_2	Silicon Dioxide
SOI	Silicon-on-Insulator
UV	Ultraviolet
XeF_2	Xenon Difluoride

1. INTRODUCTION

1.1 Motivation

Micro-electronic fabrication technology enables the construction of small mechanical devices for a range of applications. The development of such microelectromechanical systems (MEMS) by various research groups has enabled technologies with low power consumption, better device parameters, and low production cost. Each MEMS transducer may have its advantages and disadvantages over their larger counterparts.

The majority of micromachined devices move in plane with the wafer surface due to the planar fabrication technology. The focus of this thesis is to present an out-of-plane micromachined magnetic force actuator to function as a micro-mirror. Magnetic actuation has the advantage of lower voltage requirements, the capability of large force generation, and large actuation displacement when compared to many other actuation mechanisms. An affordable fabrication process is developed to build the actuators using microfabrication technology. A reflector array is fabricated in order to test the consistency of the fabrication process and actuation distance.

1.2 Organization of Thesis

Chapter 2 will introduce microelectromechanical systems and discuss the technology that enables microfabrication. Background theory on thermal, electrostatic and magnetic actuation are discussed in this section. Several different micro-mirror and Lorentz force actuators are presented to allow for performance and fabrication comparisons. This chapter also discusses a method to introduce mechanical stress into the microstructures in order to allow initial out-of-plane deflection.

Chapter 3 discusses the design concept for the stressed magnetic micro-mirror and how different forces act on the micro-mirror device. A mathematical comparison between thermal, electrostatic and magnetic forces is presented.

Chapter 4 presents the evolution of a suitable fabrication method for the micro-mirrors. The advantages and disadvantages of using different materials and fabrication methods are discussed.

Chapter 5 explores further the fabrication method chosen for the construction of the micro-mirrors. The consistency of the fabrication is discussed by examining the initial rest angles of the micro-mirror devices. Problems with using a silicon sacrificial with the fabrication method are discussed.

Chapter 6 investigates the actuation of the micro-mirrors in order to characterize their performance. The micro-mirrors are tested thermally and magnetically to observe the contribution of each force. The frequency response and lifetime of the micro-mirrors are also investigated.

Chapter 7 provides concluding remarks on the overall performance of the magnetic micro-mirror and fabrication process, as well as suggests improvements for future work.

2. MICROFABRICATION AND MEMS

This chapter provides background on microelectromechanical systems, microfabrication techniques and micro-mirror devices. If the reader has a good understanding of the topics it is recommended to skip ahead to Chapter 3.

2.1 Microelectomechanical Systems

Microelectromechanical systems (MEMS) refers to the broad field of micromachined structures developed using microfabrication techniques. MEMS are typically divided into two separate types of transducers, sensors and actuators. Sensors measure stimulus from the environment and provides a particular response that can be recorded. Actuators typically refer to devices that convert one form of energy, such as electrical energy, into mechanical motion. MEMS transducers can also be further subdivided into categories based on the predominate form of energy used in the device. The most common categories of MEMS transducers are electrical, thermal, magnetic, mechanical, radiant and chemical [1]. In some cases a device might not fit these categories or may extend over several depending on the complexity of the system.

Microfabricated systems can offer several advantages in performance, reliability and cost due to their small physical volume and weight. Since MEMS structures are fabricated with similar technology as is used in integrated circuit (IC)

technology, it is possible to integrate MEMS devices with on-chip electronics[2]. Due to their low mass, MEMS devices can have lower actuation power when compared to their larger counterparts. The size of MEMS devices also gives them high thermal sensitivity and fast actuation speeds, which may be desirable for some applications. Another advantage of MEMS is the potential for large cost savings because they are batch fabricated, and due to their size, hundreds of devices can be fabricated on a single wafer.

Despite all the advantages of MEMS devices, there are several disadvantages in implementation. Though cost savings are possible, often 50-80% of the overall cost is in the packaging of the MEMS devices [3]. Another issue is that typically the entire system is not truly small because of the power supplies and computer systems sometimes required to drive and test the system. There is research going into the potential of on-chip power supplies, some which may extract sufficient power extracted from the environment [4]. Material properties can also be difficult to control since thin film mechanical properties are not completely understood as bulk materials. Stress issues in the films can also exist which can cause undesirable device operation.

There are several different applications for MEMS in various commercial and research fields. This technology can be very attractive in such applications as communication satellites where weight, size and cost reductions are necessary [5]. In RF applications, the characteristics of MEMS devices can also make terrestrial-based communication systems more efficient with their lower insertion losses at high GHz

frequencies as well as power reduction [6]. The automotive industry has been using MEMS sensors for a number of years in such components as safety systems, engine management, suspension and braking [7]. Future MEMS applications will drive the way for higher density storage devices, more affordable diagnostic equipment in hospitals, as well as assist in the development and research in other fields due to their high sensitivity.

2.1.1 Magnetic MEMS

Magnetic MEMS is a class of micromachined transducers that use magnetic or electromagnetic energy for sensing or actuating. For the most part, magnetic MEMS is still an emerging technology in terms of commercial availability when compared to other micromachined transducers as they are still in early stages of development. A few exceptions exist, such as Hall effect sensors common in automotive [8] and other applications, as well as magnetic read/write heads which are shipped in enormous volumes in hard drives [1]. Magnetic fields either typically generated by passive magnetic field sources (permanent magnets) or by driving a current through a coil. Magnetic MEMS devices have the advantage of lower voltage requirements and the capability of large force generation and large actuation displacement. This is due to the continuous generation of fields from permanent magnets without external energy requirements.

There are several different magnetic actuating MEMS at different stages of development. In telecommunications, micromagnetic latching switches have recently

been realized using a micromachined cantilever, an active coil and a permanent magnet [9]. This technology is able to provide advantages such as cost, zero off-state power, and higher isolation. However, some tradeoffs exist such as switching speed and life cycles. Biomedical applications may also benefit from magnetic MEMS with microfludic analysis through separation of chemicals which have magnetic moments, such as deoxygenated hemoglobin [10]. As with many MEMS device, research has also gone into devising ways to miniaturize macroscale devices, such as magnetic motors [11]. A few magnetically actuated micro-mirrors have also been fabricated, and they will be discussed in section 2.3.

2.2 Microfabrication Techniques

The technology that enables the fabrication of micro-electro-mechanical systems is commonly referred to as microfabrication. Since the late 1960's, researchers realized that the technology that surrounds the development of integrated circuits could be used to develop miniature size actuators and sensors [1]. As the technologies that drive microfabrication are developed, so too are the potential devices that the processes can fabricate. This chapter will provide the reader with information on these techniques, as well as some limitations these processes place on the design.

In this thesis several microfabrication techniques are used:

- UV lithography for material patterning and photoresist sacrificial
- Thermal evaporation for aluminum and chrome deposition

- Sputtering for a silicon sacrificial material
- Wet chemical etching for aluminum/chrome etches
- Plasma etching for photoresist etching
- XeF_2 etching for highly selective silicon etching

2.2.1 Lithography

Lithography drives the development of new integrated circuits and MEMS devices. A limitation of most fabrication processes is that they are performed over the entire wafer. Lithography allows designs to be selectively patterned on different areas of the wafer. With increased development in the lithographical processes, materials can now be defined with sub-micron resolution. This process can be quite expensive depending on the resolution and complexity of the device. Since the development and fabrication of mask sets in industry can cost millions of dollars, errors in the mask are costly. In research, mask sets are typically chosen based on the amount of available financial resources and relative age of the technology being developed.

Masks are typically produced on materials such as glass or quartz since they have a high degree of optical transparency. An opaque layer is deposited on one side of the glass and then patterned to define the mask. If a device has multiple layers, each layer has its own mask. The mask set used in the fabrication of the MEMS discussed in this thesis are designed with Adobe Illustrator 10™ to scale and then the

mask is sent to a printing company[1]. These masks are produced on a transparency with a resolution of 3600 dots per inch (dpi) that translates to a resolution of 7μm. This resolution is sufficient for the design of the MEMS for this thesis, as well as affordable for quick prototyping. Once the transparency has been printed it is attached to a glass mask plate so that it can be later mounted in the mask aligner.

For this thesis, UV lithography is done using a positive photoresist. Figure 2-1 shows the mask aligner while exposing the photoresist. The contact lithography method was used throughout the project, which places the mask in contact with the resist-coated wafer. When positive resist is exposed to UV light, the photoactive compound in the resist will increase its dissolution rate when developed.

[1] GB Graphics Limited

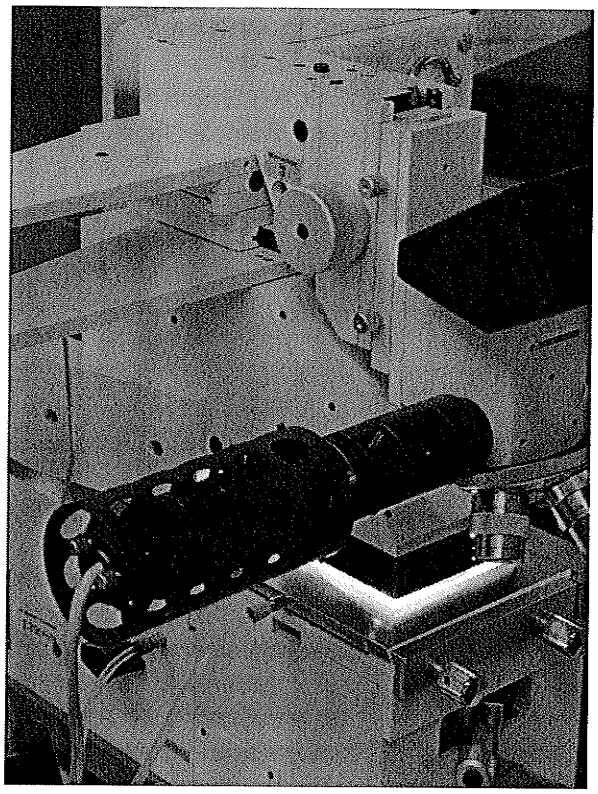

Figure 2-1. Karl Suss MA3 Mask Aligner in Operation

The mask aligner plays an integral part of the lithography process as it allows the new layers to be aligned relative to previously patterned layers. With the wafer and mask in the mask aligner, they are aligned together and then brought into contact with the wafer. Non-contact methods are generally used in industry because of the lower defect generation, however for the devices presented in this thesis the defect generation due to contact is negligible due to the relative size of the device.

2.2.2 Thermal Evaporation

Metal layers in all early semiconductor technologies were deposited by thermal evaporation. This technique is still widely used in research, however current silicon technologies use the sputtering technique because of better step coverage and better alloy deposition capabilities. Step coverage refers to the how well the deposition technique can cover the non-planar topology of the wafer. Figure 2-2 shows an example of the good and bad sidewall coverage. Deposition processes with bad sidewall coverage typically have thinner sidewalls, or if shadowing occurs the sidewall may be non-existent. Processes with good sidewall coverage tend to have uniform film thickness on the surface and sidewalls.

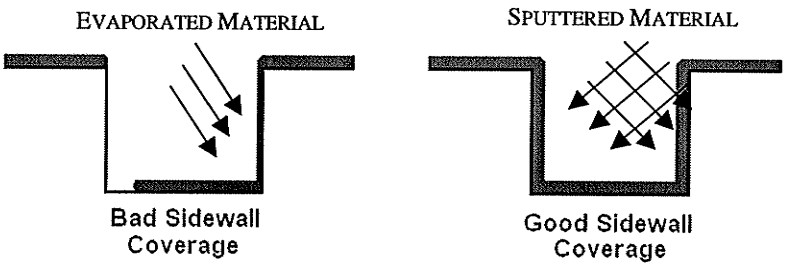

Figure 2-2. Examples of Bad and Good sidewall coverage

Thermal evaporation is performed in a vacuum chamber that is typically pumped down to a high vacuum with a diffusion or turbo pump. A charge (or source material) is placed underneath the wafers in a ceramic crucible, tungsten boat, or tungsten rod. These receptacles are chosen because they typically have a higher melting point than the charge, and do not readily react with the deposited material. Under high vacuum, the charge is heated typically by applying a current through the receptacle causing the charge to give off vapor. Since the pressure is quite low, atoms of the vapor have a large mean free path (about 50 meters at high vacuum) and travel

in a straight line from the charge until they strike a surface. Since materials have different vapor pressures it is difficult to make consistent alloys, even with separate receptacles heated to different temperatures. A schematic of thermal evaporator system used in this project can be seen in Figure 2-3.

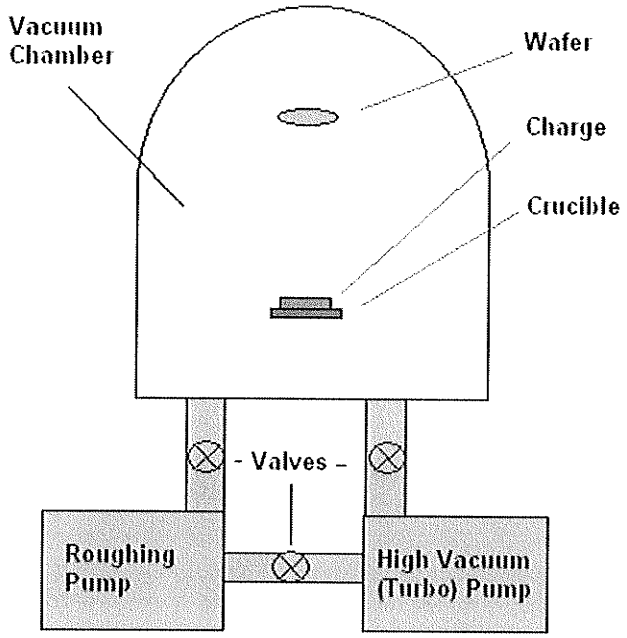

Figure 2-3. Schematic of a Thermal Evaporator System

2.2.3 Sputtering

Sputtering is an alternative to evaporation for thin metal film deposition in microfabrication. This technique was demonstrated in 1852 [12], and has many advantages over thermal evaporation that makes it the deposition method of choice in microelectronic fabrication.

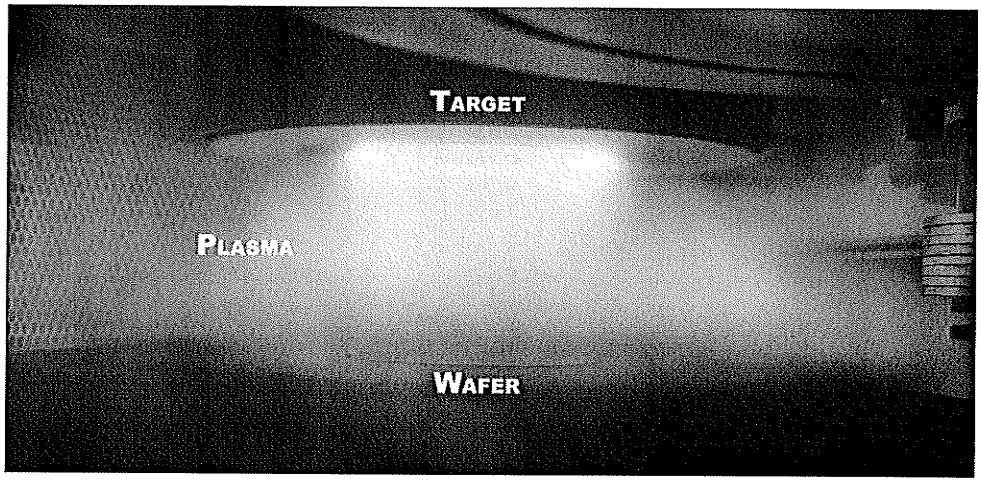

Figure 2-4. Sputtering at the University of Manitoba's Nano-system Fabrication Laboratory (NSFL)

Wafers are placed underneath the target (source material) and is pumped down to a high vacuum (10^{-6} Torr) to insure low contamination (Figure 2-4). An inert gas, such as argon, is then supplied to the chamber at a given flow rate. A large voltage, typically a few hundred volts, is then placed between the cathode (target) and the bottom electrode (wafer holder) in order to ignite the plasma. The argon ions in the plasma are then accelerated towards the negatively charged cathode. If the ions strike the target with sufficient energy, an atom will be sputtered from the target onto the wafer surface. Typically, a magnet is placed behind the target in order to increase the ion densities at the target. This technique is commonly referred to as magnetron sputtering. The targets are water-cooled since much of the power in the plasma tends to dissipate in the form of heat at the target.

Sputtering offers better step coverage than thermal evaporation, mainly due to the higher deposition pressure and the atoms being ejected with 100 times more

energy than evaporated atoms [13]. These atoms tend to have more surface mobility which also improves coverage. The higher deposition pressure makes the mean free path on the order of a few hundreds of micrometers which equates to better sidewall coverage. There are also more control parameters that allow you to achieve different characteristics with the thin films, such as gas flow, deposition pressure, and sputtering power.

2.2.4 Wet Chemical Etching

Wet chemical etching can be performed when a fabrication step requires removal of a deposited material in order to define a particular pattern on the wafer. Though slightly more established than other etching techniques, wet chemical etching has some serious drawbacks. These drawbacks include lack of anisotropy, poor process control, and excessive particle contamination. Anisotropy is a measure of how fast a particular etch etches in the lateral direction with respect to vertical etching, where perfect anisotropy means no lateral etching. Lateral etching is commonly referred to as underetching (Figure 2-5). Despite all the disadvantages of wet etching, some etches can be highly selective when compared to other forms of etching [13].

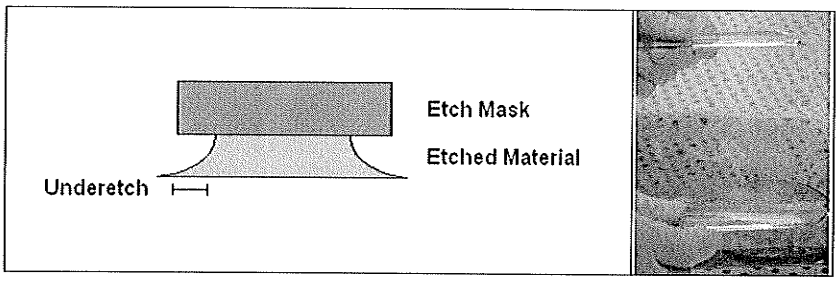

Figure 2-5. An example of underetching that occurs with wet etching (left). A wet etch performed in the microfabrication lab at the NFSL (right).

Aluminum and chrome were used extensively throughout this project and therefore an aluminum etch and a chrome etch are required. These wet etchants are quite selective to the desired etch material and therefore etch rates of other materials is assumed to be non-existent [14]. The composition of the aluminum and chrome etch can be seen in Table 2-1. Arch Chemicals supplied the various wet etches used throughout this project.

Table 2-1. Chemical composition of Chrome and Aluminum Etches

Chrome Etch	
Ceric Ammonium Nitrate	15%
Nitric Acid	5%
Water	80%

Aluminum Etch	
Phosphoric Acid	70%
Acetic Acid	10%
Nitric Acid	2%
Water	18%

2.2.5 Plasma Etching

Plasma etching is typically the preferred method of etching in industry because of several significant advantages over wet etching. In plasma etching, a feed gas is introduced into the etch chamber and broken down into chemically reactive species. The plasma-generated reactive species must then diffuse to the wafer and be absorbed for the reaction to occur. Once the reaction occurs, the byproduct must be desorbed and diffuse from the wafer and leave the etch chamber. Typically for silicon etches, a fluorinated gas is chosen as a feed gas such as carbon tetrafluoride (CF_4). For photoresist and other organics oxygenated (O_2) feed gases are chosen.

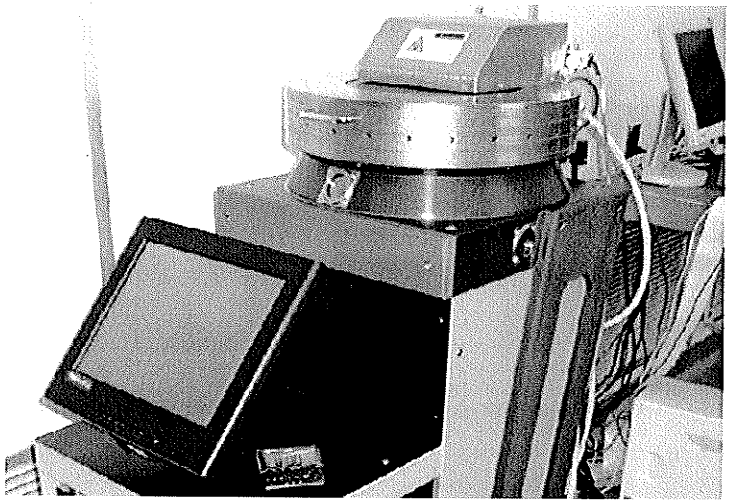

Figure 2-6. Plasma Etcher at the University of Manitoba's NSFL Cleanroom

Plasma etching is much easier to start and stop and therefore processes are typically more repeatable than wet etching. Wafers are typically placed on a water-cooled chuck to reduce temperature variations across the wafer, which allows more uniform etching. Plasma etching is also considered a cleaner process since there are

far fewer particles than in a wet etch. Gas flow rate, plasma power, and chamber pressure are just a few of the variable etch controls one may vary to achieve a suitable etch profile. Some plasma etching systems contain an inductively coupled plasma (ICP) power source to allows for additional control of the plasma generation.

2.2.6 Xenon Difluoride Etching

Xenon Difluoride (XeF_2) is a chemical used primarily to etch silicon due to its high selectivity between silicon, and other materials such as SiO_2, metals, and other insulators. An advantage of this fluorine-based etch is that it does not require a plasma generation or heating, therefore there are fewer control parameters. Xenon difluoride exists as a white crystalline solid at standard pressure and temperature, and has a sublimation pressure of approximately 4 Torr. In its gaseous form, xenon difluoride etches silicon isotropically. Removing water vapor from the etching chamber is important since any water vapor and xenon difluoride will form hydrofluoric acid which is not only a safety hazard, it will also etch any exposed oxide. Xenon difluoride also does not etch aluminum or photoresist, however slowly etches silicon nitride [14]. One disadvantage of XeF_2 etching is that it leaves a very rough surface on the silicon after the etch [13].

Its difficult to define a specific etch rate for XeF_2 etching since its dependant on several factors such as silicon loading, the size of the etch chamber, etching pressure and amount of XeF_2 gas in the chamber. When etching large areas, silicon loading causes the etch depth of a hole to be reduced when there is an adjacent etch

hole [15]. Etch rate at lower pressures is linearly proportional to etching pressure. XeF_2 can be modeled as a fluorine source, however XeF_2 etches 10^4 times faster than fluorine gas alone. The chemical reaction describing the etch is as follows:

$$2XeF_2 + Si \longrightarrow 2Xe + SiF_4 \tag{2-1}$$

The XeF_2 etching system consists of an etch chamber, expansion chamber, pump, valves, and source gasses as seen in Figure 2-7. The expansion chamber is necessary in order to increase the volume of XeF_2 gas available when the valve connecting the etch chamber and expansion chamber is opened. All silicon etching performed in this project is done by quickly pulsing the valve between expansion chamber and the etch chamber and then etching for approximately 90 seconds. The reactants are then pumped out by opening the pump valve for 30 seconds until a lower vacuum is achieved. The valve connecting the expansion chamber and etch chamber is again pulsed and the cycle continues until the etch is complete. The XeF_2 valve is kept open in order to maintain a supply of XeF_2 to the expansion chamber. This procedure will be referred to as the "Quick Pulse Method" in following chapters. For a complete process flowchart and further description of the XeF_2 system please refer to Appendix A.

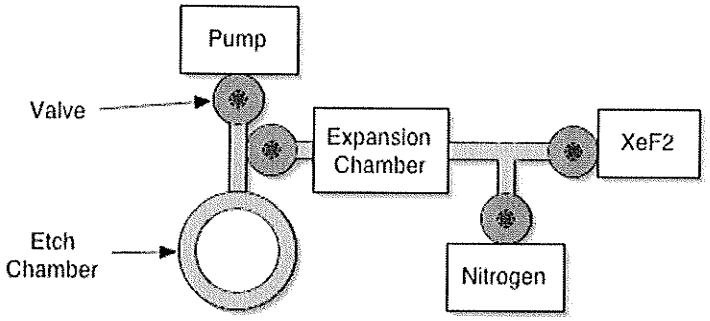

Figure 2-7. Schematic of XeF_2 System used in this project

2.2.7 Sacrificial Materials

Micromachining frequently requires a sacrificial material to be deposited, which can be later removed in order to free a device from the underlying substrate. Many materials can be used as sacrificial layers, however the key requirement of any sacrificial layer is that an etching process exists that will selectively etch the sacrificial without etching the device layer. Depending on the complexity of the design, a sacrificial layer must be chosen such that it will survive future process steps, such as metal deposition, annealing and other chemical etches the sacrificial might be exposed to. Both photoresist and silicon were considered as sacrificial materials in this thesis.

Photoresist can be used as a sacrificial material to reduce fabrication steps as well as reduces cost and fabrication time. Using photoresist as a sacrificial however is not trivial due to the chemistry of photoresist. Photoresists are deposited in a liquid form and later hardened with thermal processes commonly referred to as soft and hard baking. Photoresists typically have three main components: a resin, a

photoactive compound, and a solvent which controls the mechanical properties of the material during lithographic processing [13]. After the photoresist is exposed to the ultraviolet light and developed, thermal processing becomes important. It is desirable to reduce the solvent content of the sacrificial photoresist in order to reduce or prevent any out-gassing. If the solvent in the photoresist is not sufficiently removed, out-gassing will cause bubbles in the device layer. Soft baking is generally done on a hot plate for one minute at around 110°C in order to reduce some of the solvent content (usually to about 5% original concentration) and prepare the wafer for UV lithography exposure [13]. Hard bakes are typically done after lithography and developing in order to further harden the resist. This is done by placing the wafer on a hot plate or in an oven for a set amount of time depending on photoresist thickness. Figure 2-8 shows the general process flow of photoresist patterning.

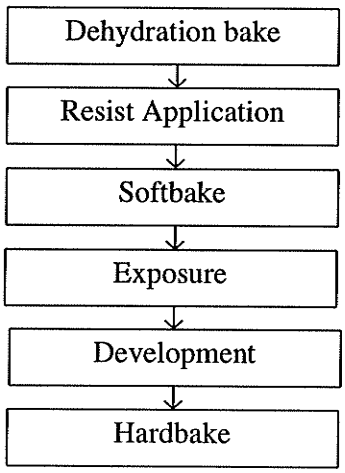

Figure 2-8. Photoresist patterning process flow

There are several different methods for etching the sacrificial photoresist. The most common methods to remove photoresist are oxygen plasma etching or wet

etching with acetone. Acetone is able to etch photoresist quite rapidly, however a stiction problem can occur during release due to surface tension forces resulting from the trapped rinse liquid and resins [16]. This stiction problem prevents devices that have been underetched from being fully released. Some research has gone into post-release rinsing and thermal annealing in order to overcome this problem, however only limited success was reported [17]. In this paper, several post-release processes were attempted using heated bathes of water or methanol, often followed by a quick high temperature anneal. Oxygen plasma etching is preferred over wet chemical etches since there is less chance of sticking as well as more process control. Since the photoresist is quite thin under the devices, etch holes are required to decrease overall lateral etch times. This is particularly important for plasma etching since lateral etching can be 1 micron per minute or less depending on etching parameters [18].

2.3 Micro-mirrors

Micro-mirrors have many potential applications in telecommunication and personal technology sectors. Micro-mirrors can perform many functions, such as optical modulation, optical scanning, and optical filtering to name a few. Since micromirrors typically have an optical nature, they are often referred to as micro-optical-electro-mechanical systems (MOEMS). Several different designs have been implemented using electrostatic and magnetic forces for actuation. In this section a few examples of commercial and non-commercial micromirrors will be discussed to provide some comparison between current devices and the devices fabricated in this thesis [19-24].

2.3.1 Texas Instruments Digital Light Processing (DLP) Mirror

One of the most successful commercial micro-mirror implementations is the digital light processing (DLP) system from Texas Instruments that is used in cinema displays as well as high-definition television [21]. This MEMS-based technology uses electrostatic attraction to actuate the mirror, which is addressed using 5 volt complimentary metal oxide semiconductor (CMOS) static random access memory (SRAM) cell. The aluminum micromirror has angular displacement of 20 degrees from its on-state to off-state implemented with torsion hinges and central yoke. Each micromirror is approximately 16um by 16um. In order to achieve 256 grayscale levels, each micromirror pixel is controlled with an 8-bit word that specifies the time

in each state. The metal layers are deposited using sputtering, and an organic sacrificial is spin-coated to later form the underlying air gap. A simple schematic of an individual mirror element can be seen in Figure 2-9. To create an image, each mirror is exposed to a cycle of primary colors (red, green, blue) and is reflected either towards or away from a projection lens.

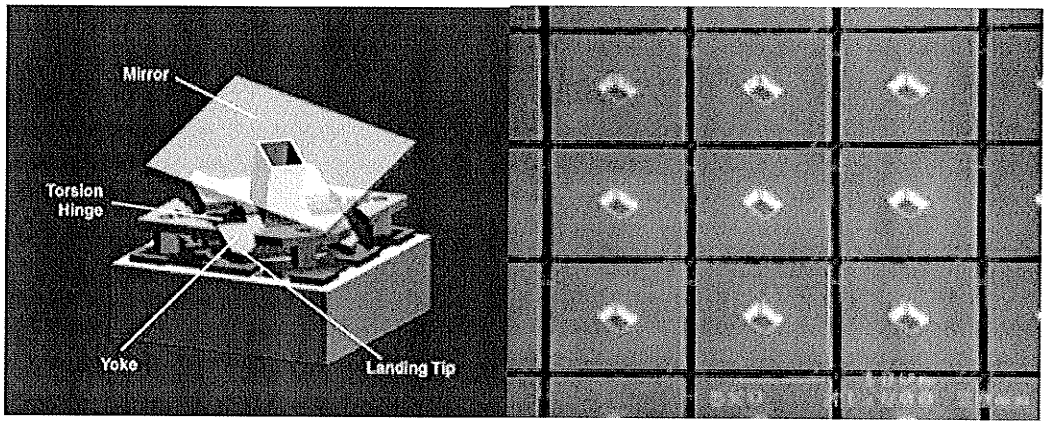

Figure 2-9. Schematic pixel and array of Texas Instrument's DLP System [21]

2.3.2 Seoul National University Micro-mirror

Another example of a micromirror system is the electromagnetic micro-mirror design by the Seoul National University [23]. The design consists of a 300x300μm aluminum micro-mirror deposited and etched on the silicon substrate in order to maintain a flat mirror surface. Nickel is electroplated on the sides of the mirror to provide a magnetic actuation mechanism. Thin aluminum crab-leg springs hold the micro-mirror in place when it is released from the bulk substrate. Silicon thicknesses ranging from 10 to 20μm were chosen for the structural support of the micro-mirrors. In order to release the support silicon from the bulk, a back-side potassium hydroxide

(KOH) wet etch is performed until the desired thickness is achieved followed by a front-side deep reactive ion etch (DRIE). A schematic of the released and actuated device can be seen in Figure 2-10. The fabricated device was tested by applying an external magnetic field, as well as simulated using an ANSYS™ simulation. The fabricated micro-mirror began actuating at approximately 0.0025 Tesla when the magnetic forces overcomes the mechanical restoration forces, and became approximately normal to the substrate at approximately 0.011 Tesla. A similar design concept was implemented using a gold-plated FeNiCo/poly-silicon micro-mirror for a fiber-optic cross-connect, where upon actuation of the incoming optical signal was reflected and coupled into another fiber [25].

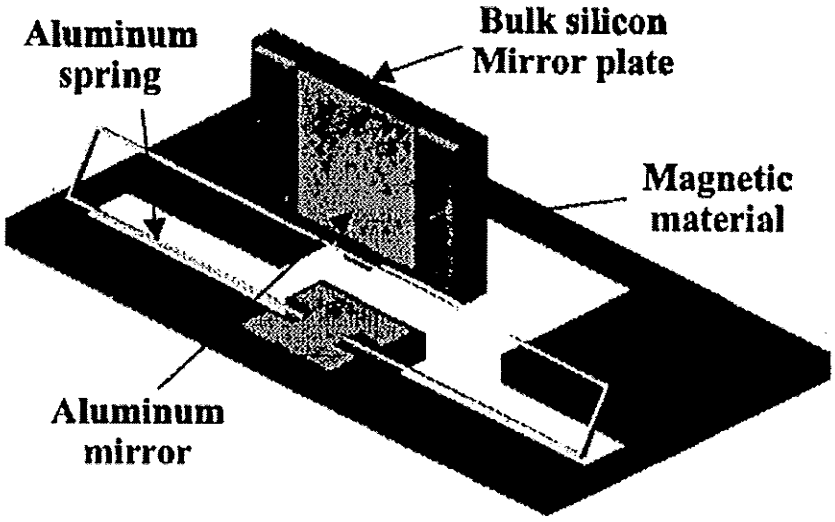

Figure 2-10. Schematic of Electromagnetic Micromirror [23]

2.3.3 Electrostatic/Magnetic Latching Micro-mirrors

Micro-mirrors using a combination of magnetic actuation and electrostatic latching have also been developed for optical switching [26]. A 8x8 port MEMS-based fiber-optic switch was created using two separate chips: a bottom chip which contains the array of fabricated micromirrors and the top chip which is used for alignment and for electrostatic latching. An image of the layout of a single micromirror element on the bottom chip can be seen in Figure 2-11. The two chips are later flip-chip bonded together during the final assembly process. The micromirrors are positioned at a 45° angle to the input and output fibers, thereby reflecting the input fiber beam into the addressed output fiber. The micromirrors are fabricated a silicon-on-insulator (SOI) wafer. The gold reflector, chosen for its high reflectivity at IR wavelengths, is deposited on the oxide after performing a plasma etch on the thin device-layer silicon film. Polysilicon torsion hinges are deposited to attach the mirrors to the wafer as well as provide an electrical connection. NiFe pads are electroplated on both sides of the micromirror, however are mechanically isolated from the mirror structure due to the high stress in the films. The top chip is constructed by etching deep slots through a <110> silicon wafer using a wet anisotropic KOH etch.

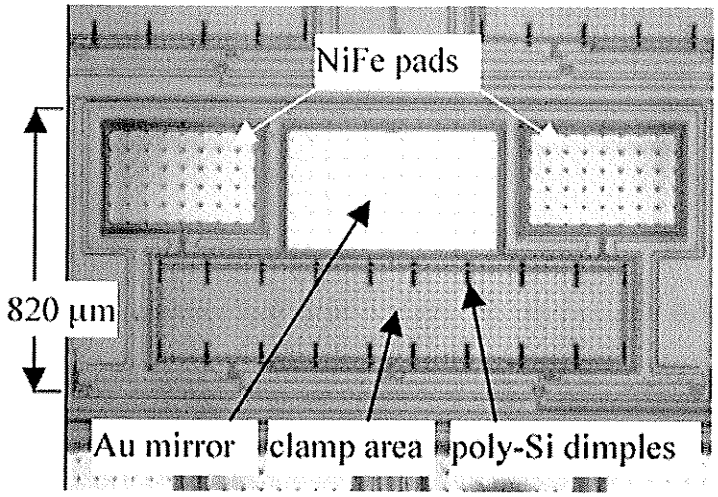

Figure 2-11. Layout of magnetically actuated optical switch

In order to latch the micro-mirror vertically or horizontally, the top chip is biased at a given voltage while the bottom chip remains grounded (Figure 2-12). To lift a micromirror vertically, the micro-mirror is grounded to allow movement when an external magnetic field is applied. If the micro-mirror is biased to the same voltage as the top chip, the electrostatic forces will prevent the device from moving. Once the micro-mirror is vertical, it will latch to the sidewall of the top chip through electrostatic forces when the magnetic field is removed. These micro-mirrors are able to show high repeatability across the array (0.003 degrees difference), with this variation coming largely due to sidewall surface roughness. Switching times of 8.5ms were achieved with insertion losses on the order of 1dB.

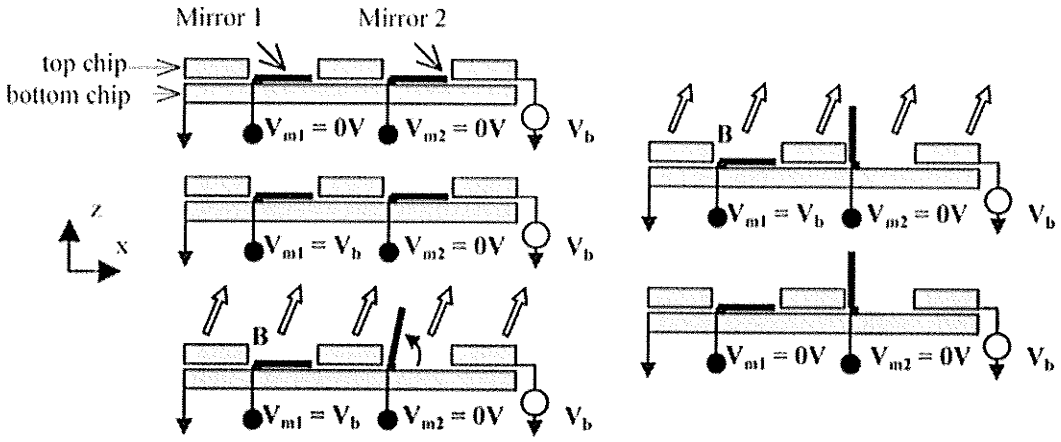

Figure 2-12. Switching sequence of magnetically actuated optical switch

2.3.4 Lucent LambdaRouter

Another commercial micro-mirror is the electrostatic LambdaRouter fabricated by Lucent (Bell Labs) [22]. This device uses a combination of micromachined springs and electrostatic attraction in order to provide biaxial actuation. Figure 2-13 shows the one of the micromirrors of the LambdaRouter under actuation. When these micro-mirrors are used as part of an optical cross-connect (OXC) system, they can achieve peta-bitrates which is approximately 1000 times faster than their electrical counterparts.

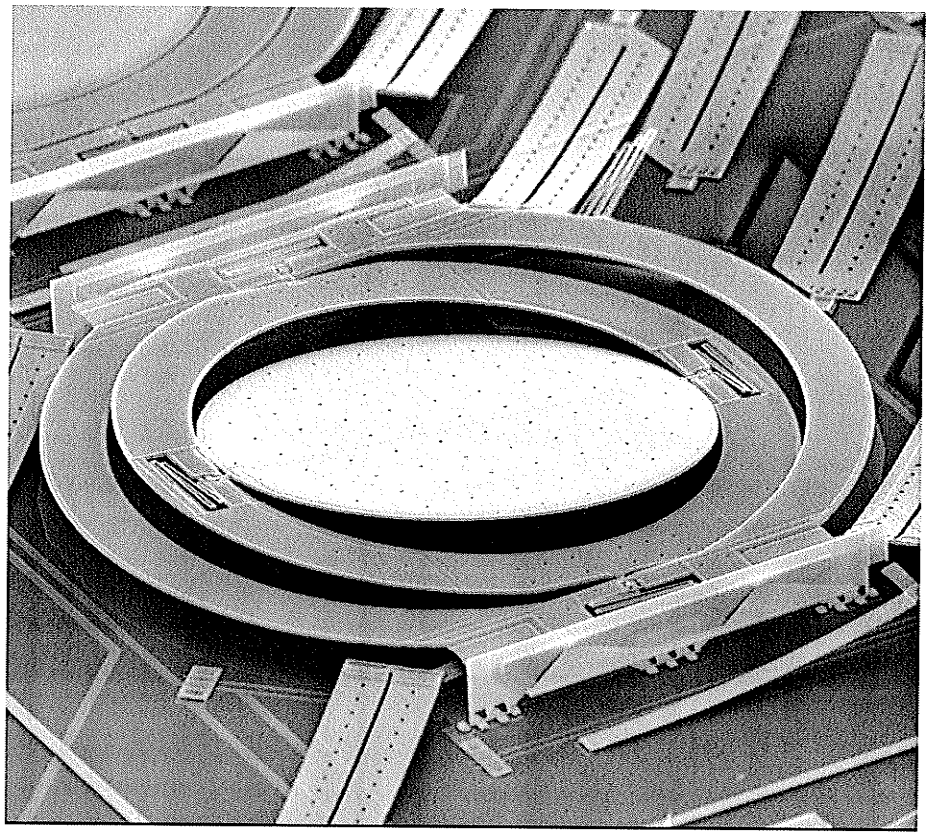

Figure 2-13. Lucent LambdaRouter Micromirror [22]

2.4 Single Loop Lorentz Force Actuators

Lorentz force actuators have been previously fabricated using a simple released current loop structure for self-assembly and micro-grid movement applications [27, 28]. Lorentz forces are generated whenever a current is in the presence of a magnetic field, and follows the following equation:

$$F = Current \times Length \times MagneticFluxDensity = ILB \tag{2-2}$$

Single loop structures were fabricated for self-assembly on a thin SiO_2 layer to provide insulation between the fixed pads [27]. Devices used for self-assembly are fabricated using a chrome seed-layer with a thick 4 μm electroplated copper layer on a silicon sacrificial layer. An example of the simple loop structure created for the self-assembly structures can be seen in Figure 2-14. By performing self-assembly with Lorentz forces you are able to position the structure without making direct contact with the released structures, and requires less dexterity from human operators using micromanipulators. This self-assembly technique was used to assemble a box structure.

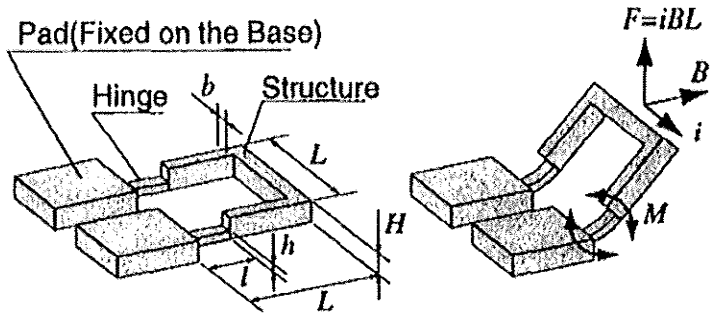

Figure 2-14. Schematic of Self-Assembly Single Loop Lorentz Force Actuators [27]

The micro-grid device (Figure 2-15) was constructed with a thin aluminum device layer, and silicon sacrificial layer [28]. The springs are fabricated in-plane with the wafer surface and therefore must be micro-manipulated to be perpendicular to the wafer surface. Micromanipulators were used to place move the springs out of plane, however achieving 90 degrees deflection proved to be difficult with the structure. Applying a 20mA current to the structure displaced it approximately 10μm in both x and y directions, depending on which pads are excited.

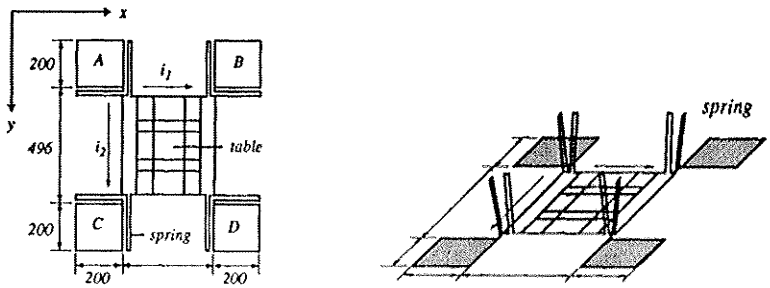

Figure 2-15. Schematic of moveable micro-grid using Single Loop Lorentz Force Actuators [28]

2.5 Lorentz Force Micro-mirrors

This section will provide some background on Lorentz force micro-mirrors to evaluate against the performance of micromirrors developed in this thesis.

2.5.1 2-D Lorentz Force Actuated Micro-mirrors

A micromachined bridge micro-mirror was designed and fabricated at the Technical Institute of Berlin [29]. The four-mask design started with a <100> SOI wafer, which was then etched with KOH to define the area supporting the micromirror (Figure 2-16). A 110nm thick layer of dry thermal oxide was then grown to insulate the polysilicon wires from the bulk silicon. With the oxide grown, a phosphorus-doped polysilicon layer is deposited and then patterned with a wet etch to define the flexures and the conductor loops. Aluminum was then sputtered and then patterned to form the bondpads and mirror metallization. The backside was then etched with KOH in order to release the mirror structure. The front-side of the wafer was protected with a waxed on Pyrex wafer during the KOH etch.

The performance of a 1300x1500x15μm^3 micromirror with 66μm wide and 500nm thick flexures are measured. These micromirror structures were capable of up to

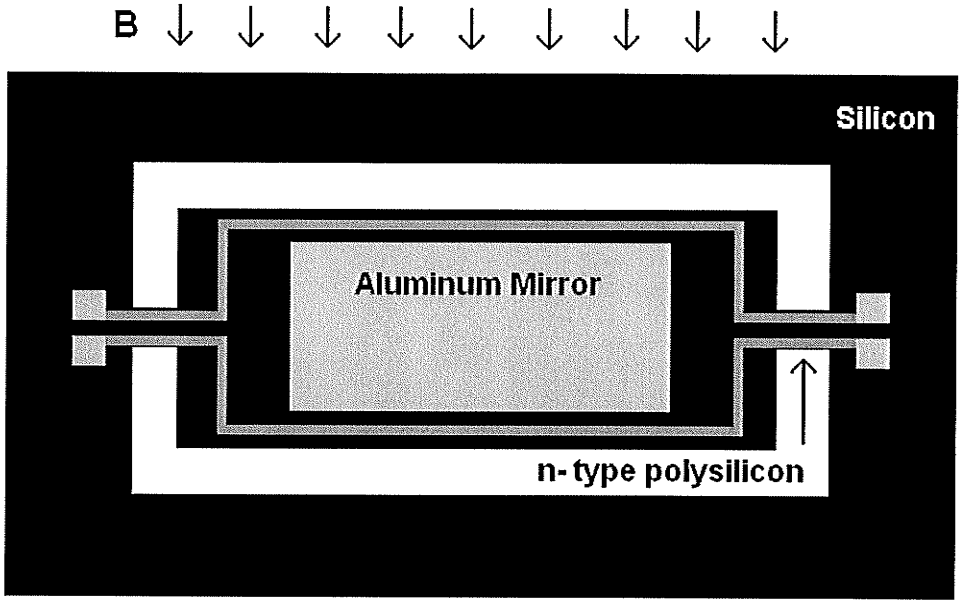

Figure 2-16. Schematic of 2-D bridge Micromirror

7° of deflection with a 1mA drive current, and 1T magnetic field. The deflection angle saturates with larger currents, as the forces generated are not able to overcome the restoring forces from the torsion in the flexures. The micromirrors resonant frequency was calculated to be 280Hz using finite element analysis. Another example using this technique was used to achieve two axis mirror rotation with polyimide flexures, and achieved a deflection 23° with a 29mA current and a 0.24T magnetic field [30].

2.5.2 Laterally Driven Electromagnetic Microactuators

A lateral drive electromagnetic microactuator was designed and fabricated into a micro-optical switch application [31]. A beam structure with leaf springs is

actuated with Lorentz forces to move a shuttle with a micromirror positioned at the end (Figure 2-17). A permanent magnet is placed under the silicon wafer to provide the magnetic field used to move the structure. Switches were fabricated a silicon wafer, with a 3μm LPCVD (low pressure chemical vapor deposition) oxide used as an insulating layer. The device layer consisted of a 16μm n^+ polysilicon, deposited by stacking 2μm polysilicon layers using LPCVD. An oxide is deposited on the device layer to function as a dry etch mask for reactive ion etching used to achieve the high aspect-ratio polysilicon structures. The oxide under the structures was etched using a buffered hydrofluoric acid (HF) solution. A thin layer of aluminum is then sputtered on the polysilicon to improve reflectivity of the micromirror and to enhance the electrical conductivity along the leaf springs. The entire fabrication process was completed within 24 hours.

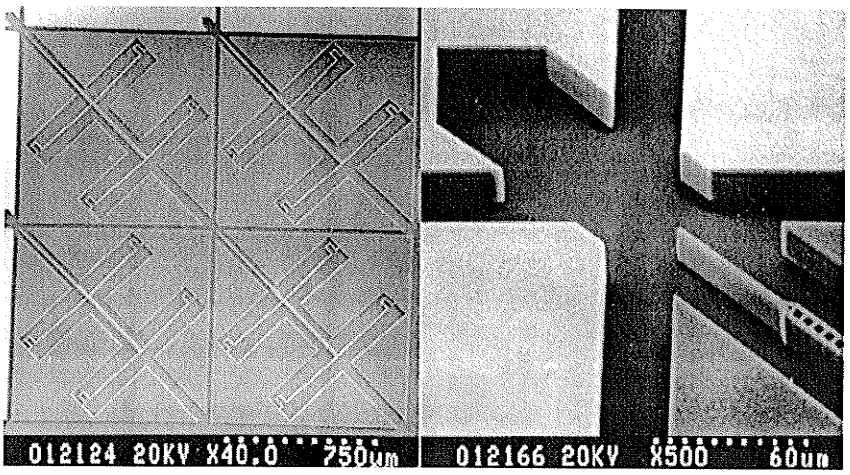

Figure 2-17. Micro-switches using Laterally Drive Electromagnetic Microactuators [31]

A 0.3T permanent magnet was placed under the silicon wafer for testing purposes. The performance of a leaf spring was measured which had a width, thickness, and length of 1.2, 16, and 920μm, respectively. The resistivity of the spring was measured to be approximately 5 ohms. The leaf spring deflected at a slow linear rate until the springs engaged at around 400mA (15μm deflection). With the springs experiencing snap-through, a deflection of 60μm was recorded at 566mA. A 1m high free drop test was performed to test robustness of the structures. After the drop test the micromirror was actuated over a million times with no signs of structural fatigue.

2.6 Thin Film Stress

When stress is applied to a material, it exhibits strain proportional to the stress. Each material has different stress properties that govern how the material will respond when it undergoes strain. Once a material has been stressed above its yield stress, the material will deform significantly and will exhibit permanent deformation when the stress is removed. If the material goes beyond its ultimate stress, the material will fail and typically break into separate sections. Ductile materials that bend before they break, usually have an ultimate stress much larger than the yield stress. Brittle materials that break before they bend, typically have ultimate stresses much lower than yield stresses.

For thin film materials, the material stress properties are usually governed by the deposition parameters, such as deposition rate, pressure and temperature.

Materials can exhibit some intrinsic stress due to the variation in the crystalline structure of the deposited layers. Two materials deposited on each other can also exhibit strain when released due to residual stress within each material. For example, chrome tends to have residual tensile stress when thermal evaporated [32]. Knowledge of the characteristics of the deposited film allow for strain cancellation, or give the composite thin film an inherent stress. This inherent stress can bend the beams up or down depending on the difference in residual stress between materials. This technique was used to fabricate a microwave switch with high isolation [33], as seen in Figure 2-18. The switch consists of a 0.5μm thick aluminum film coated with 0.1μm chrome deposited using electron beam evaporation. The curvature of the structure changes depending on the thickness ratio of the two metals.

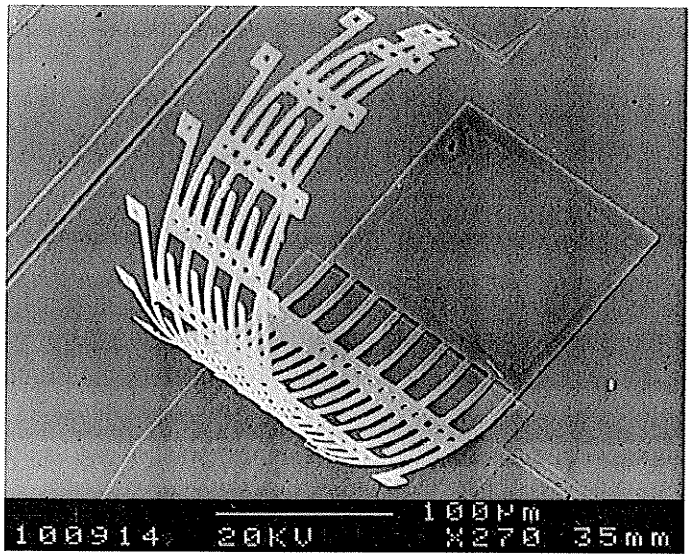

Figure 2-18. Microwave switch fabricated with aluminum stressed with chrome [33]

A structure may experience plastic deformation when the yield strength of the material is exceeded when stressed. The elastic-to-plastic transition angle can be estimated by determining when the applied torque T applied is equal the yield moment (M_y) of the beam [34]. For a simple beam structure, the yield moment is defined as

$$M_y = \frac{\sigma_y w_m t_m^{\,2}}{4} \tag{2-3}$$

where σ_y is the yield stress of the material, w_m is the width of the beam, and t_m is the thickness of the beam. The yield stress of the material may be determined using a material handbook, or experimentally. The yield stress of thin films tends to be highly dependent on deposition condition.

The relationship between the torque T, and angle (θ) in the elastic regime

$$T = \frac{E_m I_m}{L_m}\theta \tag{2-4}$$

where L_m is the length of the bending regime, E_m is the Young's modulus of the material, and I_m is the moment of inertia of the structure. By equating equation 2-3 and 2-4, the angle that the structure switches regimes may be approximated by

$$\theta_{elastic-plastic} = \frac{\sigma_y w_m t_m{}^2 L_m}{4 E_m I_m} \qquad (2\text{-}5)$$

3. DESIGN AND MODELLING OF MAGNETIC MICRO-MIRRORS

Many micro-machined devices typically lay parallel to the wafer surface in an non-actuated state because of the planar fabrication technology. However, it might be favorable to have a structure lie at a given angle away from wafer surface for applications such as diffraction gratings or optical switches. The initial rest angle of the micro-actuator facilitates improved underetching of the micro-mirror structure.

3.1 Design concept

In order to achieve an out-of-plane initial position for the micro-mirror, it is possible to induce residual stress into the device. This can be achieved by depositing different metals on a single structure, which typically causes stress at the metal-metal interface. This technique of using residual stress of deposited materials was recently used to fabricate a microwave switch with high isolation on its 'off' state (Figure 2-16) [33].

The magnetic microactuator in this thesis can be modeled as a current loop as seen in Figure 3-1. A current is passed through this loop in the presence of a magnetic field. Similar single coil Lorentz actuators exist, however they do not incorporate a bimetallic structure for initial position or require micromanipulation [27, 28]. Lorentz forces generated in the loop will deflect the actuator, assuming there is an initial lift angle

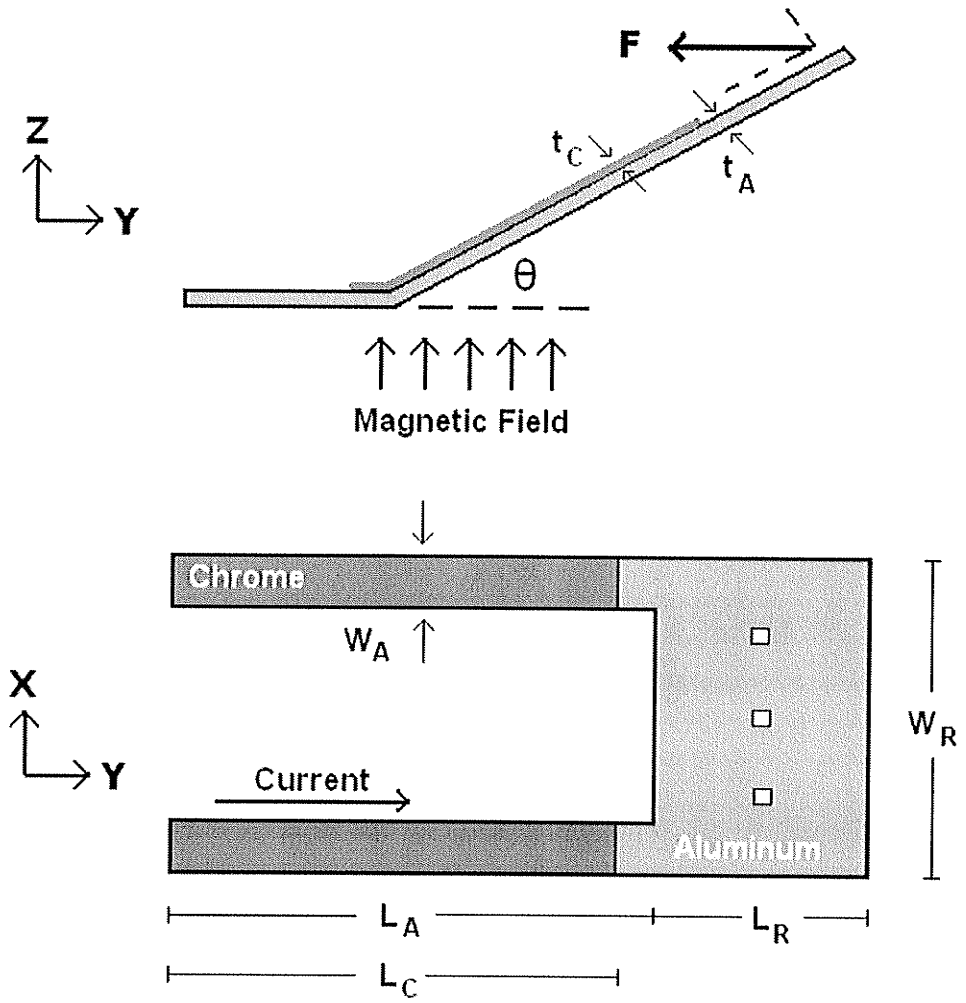

Figure 3-1. A simple schematic of the proposed magnetic microactuator

from the stress induced by the deposited chrome. This thin film stress is difficult to determine a priori due to variability in deposition parameters and film characteristics when thermally evaporating thin films. Due to this variability, a large number of test structures were fabricated with varying width, height, structure, and chrome length. The various length, widths and thicknesses used in the initial test fabrication are seen in Table 3-1. Etch holes are placed in the reflecting pad to facilitate faster

underetching. The base of the flexure is attached to a contact pad that adheres the reflector structure to the wafer surface.

Table 3-1. Geometric Design Parameters of the Stressed Magnetic Actuators

Aluminum Thickness t_A	0.5 – 1μm
Chrome Thickness t_C	50 – 100nm
Flexure Width W_A	28, 56μm
Reflector Width W_R	200 - 750μm
Flexure Length L_A	100 – 1000μm
Chrome Length L_C	0 – 1000μm
Reflector Length L_R	100-900μm

3.2 Actuation Mechanisms

The following sections will introduce several equations and actuation mechanisms that are expected to govern the actuation and characteristics of the micromachined micro-mirror. When driving a current through the micro-mirror, it will actuate due to thermal stress, magnetic forces, and electrostatic forces. Power that is dissipated in the form of heat will cause the bimetallic structure to actuate thermally. Magnetic forces are generated from the current which passes through the structure in the presence of a magnetic field. Electrostatic forces exist between the released actuator and the substrate if a large voltage bias is applied or if one of the structures has been charged. The following sections will explain how these forces will affect the micromirror structure presented in this thesis.

3.2.1 Material Properties

The material properties of thin films have to be considered in order to model the characteristics of the stressed magnetic actuators. Thin film properties tend to vary depending on deposition conditions, however, a first-order approximation is to assume they are similar to the bulk materials. Table 3-2 shows the material properties of aluminum and chrome used to model the structures.

Table 3-2. Bulk Material Properties of Aluminum and Chrome

	Aluminum	**Chrome**
Young's Modulus (GPa) [35]	70	140
Thermal Conductivity (W/mK) [36]	237	90
Thermal Expansion Coefficient (1/K) [36]	25×10^{-6}	6×10^{-6}
Resistivity (Ohm/m) [35]	26×10^{-9}	1.3×10^{-7}

3.2.2 Thermal Expansion

When current is driven through any system, heat is generated in resistive elements. This phenomenon can be used in a number of ways in order to actuate micromachined structures through thermal expansion. Thermal expansion is the tendency of a material to increase or decrease in size when heated. Each material has a different thermal expansion coefficient, α_T, and therefore different materials will expand at

different rates. For moderate temperature changes for aluminum, the thermal expansion coefficient can be assumed linear with respect to temperature. Therefore we may write

$$\Delta L = L_A \alpha_T \Delta T \tag{3-1}$$

where ΔT is temperature change and L is the initial length at a given temperature. The rate at which the device heats and cools will govern the switching speed of thermal actuation. For a bimetallic cantilever structure it can be shown that the radius of curvature is [37]

$$R = \frac{(b_1 E_1 t_1^{\,2})^2 + (b_2 E_2 t_2^{\,2})^2 + 2 b_1 b_2 E_1 E_2 t_1 t_2 (2 t_1^{\,2} + 3 t_1 t_2 + 2 t_2^{\,2})}{6 b_1 b_2 E_1 E_2 t_1 t_2 (t_1 + t_2)(\alpha_2 - \alpha_1)\Delta T} \tag{3-2}$$

where E_X is the Young's Modulus, b_X is the width, and t_X is the thickness for each respective material. For small deflections it can be shown that the deflection, d, at the end of the beam is as follows [37]:

$$d = \frac{1}{2R}(L_A + L_R)^2 \tag{3-3}$$

Conduction, radiation and convection are three mechanisms for thermal heat transfer. Conduction occurs when more energetic particles transfer their energy to

nearby atoms or molecules which are less energetic. The one-dimensional conduction heat transfer rate along length L_A given by:

$$Q_{cond} = \frac{kWt\Delta T}{L_A} \tag{3-4}$$

where k is the thermal conductivity of the material, W is the width, t is the thickness, and L_A is the length of the flexure.

Convection is the thermal energy transfer between a solid surface and a gas or liquid in motion. Convective heat transfer is therefore typically smaller than conductive if no gas or liquid is present (ie. in vacuum). Natural convection will also occur, which further reduces the thermal effect on the micro-mirror. Therefore, convection shall be ignored.

Radiation is negligible with the dimensions and temperatures used in this project when compared to conduction. Heat transfer from radiation may be defined as:

$$Q_{rad} = \varepsilon\sigma A_{rad}(T^4 - T_{ambient}^4) \tag{3-5}$$

where ε is emissivity (0-1), σ is the Stefan-Boltzmann constant, A is the surface area of the object, T is the final temperature, and $T_{ambient}$ is the ambient temperature (both

in Kelvin). The contribution of the ambient temperature may be ignored when the temperature difference is large; such as is the case with the micro-mirrors.

Equation 3-6 shows that heat transfer by radiation is negligible. The heat transfer ratio between conduction and radiation, assuming an emissivity of 1, an operating temperature from room temperature (25°C) to the melting point of aluminum (660.32°C), flexure thickness of 0.5μm, and flexure arm length of 1mm is:

$$Ratio_{cond/rad} = \frac{kA_{cond}\Delta T}{L}\left(\frac{1}{\varepsilon s A_{rad} T^4}\right) = \frac{k(tw)\Delta T}{\varepsilon s(2Lw)T^4 L} = \frac{kt\Delta T}{2\varepsilon s T^4 L^2} = 0.875 \qquad (3\text{-}6)$$

This ratio shows that conductive heat transfer is almost equal to that of the radiation heat transfer at the melting point of the device metal. At the operating temperature of the micro-mirrors (near 200°C), this ratio is over 100. Since this ratio is relatively high at the operating temperature of the micro-mirrors, radiation may be ignored.

Assuming little residual stress, the displacement of the micromirror due to thermal expansion forces can be found by directly applying the bulk material properties in Table 3-2 to (3-2) and (3-3) and varying the temperature difference. Thermal conduction between the tip of the actuator and the base of the actuator can be determined by assuming that the base of the actuator is cold and the tip of the

actuator is hot (Figure 3-2). This assumption comes from the fact that the base of the actuator is adhered to the silicon wafer surface which acts as a large heat sink. From the tip to the base of the actuator there are two pathways (both flexure arms) for the heat transfer to occur, therefore

$$Q_{cond} = \frac{2kA\Delta T}{L_A} \tag{3-7}$$

The total electrical resistance of the structure comes from the flexure arms (R_A) and the reflector pad. Due to the size of the reflective pad, the greatest contribution to the

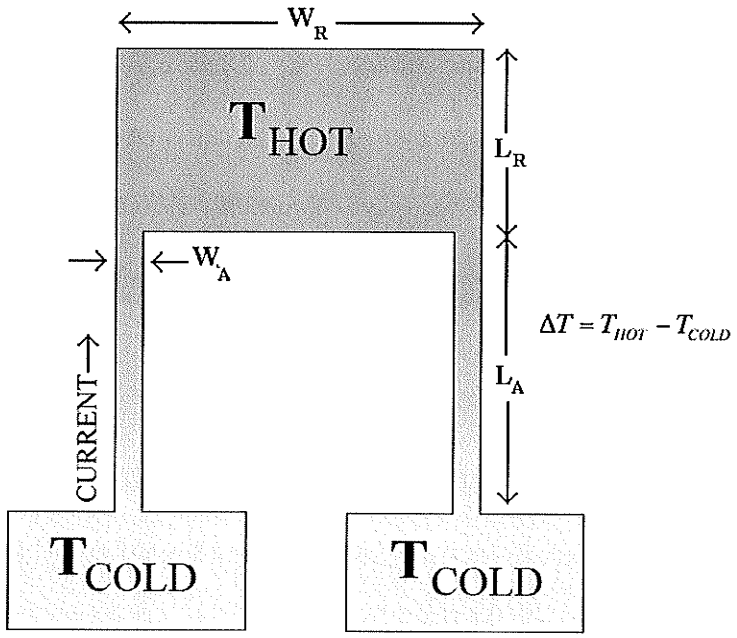

Figure 3-2. Schematic of Thermal Heating

resistance comes from the flexure arms of the micro-mirror. Resistance of each flexure arm may be written as:

$$R_A = \frac{\rho L_A}{A} \tag{3-8}$$

where ρ is the resistivity of the material, L_A is the flexure length, and A is the cross-sectional area of the flexure. Therefore the total resistance would be

$$R_{TOTAL} = 2R_A = \frac{2\rho L_A}{A} \tag{3-9}$$

since each micro-mirror has two flexure arms. The power dissipated in the system can be found the using power equation:

$$Q = \frac{I^2 R_{TOTAL}}{2} = \frac{I^2 \rho L_A}{A} \tag{3-10}$$

where I is the current through the device. Power is divided by a factor of two since heat generated has approximately an equal probability of going to the hot and cold regions.

The relationship between current and temperature difference between the reflecting pad and base may then be approximated by,

$$I = \sqrt{\frac{2k\Delta TA^2}{L_A{}^2\rho}} \tag{3-11}$$

or

$$\Delta T = \frac{I^2 L_A{}^2 \rho}{2kA^2} \tag{3-12}$$

by equating 3-7 and 3-10.

3.2.3 Lorentz (Magnetic) Forces

When charge carriers are traveling through a magnetic field they will deflect by a force commonly referred to as a Lorentz force. The Lorentz force equation is given by:

$$F = -q(v \times B + E) \tag{3-13}$$

where q is the charge of the particle (Coulomb), v is the average drift velocity of the electrons (m/s), B is the magnetic flux density (N/Am), and E is the electric field strength (V/m). Current can be defined as

$$I = \frac{q}{t} \tag{3-14}$$

where I is current and t is time. Assuming velocity is in a straight line it can be defined as

$$v = \frac{L}{t} \tag{3-15}$$

where L is the length of conduction path. By substitution, and assuming no electrostatic force, the Lorentz Force equation can be simplified to

$$F_{lorentz} = I \times LB \tag{3-16}$$

Assuming the magnetic forces will be the dominant actuation mechanism, the following model can be formulated by neglecting the thermal contribution. Torque generated by the magnetic force can be estimated by assuming a point force is exerted on the end of the structure. Torque may be defined as

$$T = Fd = FL_A \tag{3-17}$$

where F is the force exerted, and d is the distance between the force and point of rotation. This leads to

$$T = (IW_R B)(L_A)\sin\theta \tag{3-18}$$

where W_R is the reflector width, L_A is the flexure arm length, and θ is the angle of reflector at the end of the micro-mirror structure (Figure 3-1). The parameters used for force and distance are chosen to give a first order approximation of the simple micro-mirror structure. Torque may be related to angular deflection by using (2-15).

$$T = \frac{E_m I_m}{L_m}\theta \quad \Rightarrow \quad \theta = \frac{L_m T}{E_m I_m} \tag{2-15}$$

The new angle, θ_x, of the micromirror may then be determined by knowledge of the previous angle, θ_{x-1}, and the applied torque T from (3-18):

$$\theta_x = \frac{(IW_R B)(L_A)(\sin\theta_{x-1})L_m}{E_m I_m} + \theta_{x-1} \tag{3-19}$$

3.2.4 Electrostatic Forces

Electrostatic forces may need to be accounted for if a large bias voltage is placed between the reflector and the substrate, or if the separation distance between them is relatively small. With a grounded substrate, applying a voltage to the reflector will cause an electrostatic attraction which will generate a force. If this interaction is modeled as a parallel plate capacitor, the energy stored can be found by

$$W = \frac{1}{2}CV^2 = \frac{\varepsilon_r \varepsilon_o A V^2}{2d} \tag{3-20}$$

where C is the capacitance, V is the voltage, ε_r is the relative permittivity, ε_o is the permittivity of free space, A is area, and d is the distance between the plates. Force can be determined by differentiation of (3-20):

$$F = \frac{\delta W}{\delta d} = -\frac{\varepsilon_r \varepsilon_o A V^2}{2d^2} \tag{3-21}$$

For small micromirror-substrate angles, the force generated by the electrostatic force may be approximated by (3-21). The area and distance can be estimated to be that of the reflecting pad, since it makes up for over 75% of the total area of the device.

3.3 Force Comparison

Comparison between the forces allows for the analysis of which of the forces dominate the displacement of the structure under different conditions. This section will describe how a typical micro-mirror structure will respond to the various forces.

In this thesis, the 800μm x 600μm micro-mirror structure is discussed extensively and therefore will be given as an example for this discussion. This design consisted of W_A=56μm, L_R=350μm, W_R=600μm, t_A=0.5μm thick and t_C=0.1μm. Currents up to 100mA were driven through the micro-mirror structure, which had an approximate resistance of 1 ohm.

3.3.1 Electrostatic and Magnetic Force Comparison

When the structure is evaluated at a small angle the electrostatic force may be approximated by the parallel plate equation. The distance to the middle of the reflector from the base of the support arms can be found by

$$L_{mid-reflector} = L_A + \frac{L_R}{2} \tag{3-22}$$

where L_R is length of the reflector. The reflector-substrate separation may then be approximated by

$$d_{seperation} = \sin(\theta) \times L_{mid-reflector} \tag{3-23}$$

where θ is the lift angle of the micromirror.

At 100mA, the voltage on the reflector is approximately 50mV due to the highly resistive flexure arms on the 1 ohm structure. Substituting 3-23 and the dimensions of the reflecting pad to equation 3-18 gives the approximate electrostatic force at a given angle.

$$F = \frac{\varepsilon_r \varepsilon_o A_{mirror} V^2}{2d^2} = \frac{(1)(8.854 \times 10^{-12} F/m)(300um \times 600um)(0.05V)^2}{2(\sin(\theta) \times (800um - 300um/2))^2} \tag{3-24}$$

The magnetic force acting on the micro-mirror can be found by using the Lorentz force equation (3-16), taking into account the effect of the lift angle. In this thesis, a permanent magnetic with a magnetic field strength of 0.25 Teslas when measured from the silicon wafer surface, and therefore this value is evaluated in this comparison.

$$F_{magnetic} = (I \times W_R B)\sin(\theta) \tag{3-25}$$

$$F_{magnetic} = (0.1A \times (600um)(0.25T)\sin(\theta)) \tag{3-26}$$

Evaluating the electrostatic and magnetic forces at small deflection angles using 3-24 and 3-26 reveals at which point the electrostatic forces dominate (Figure 3-3). This angle is quite small (less than 0.1°) due to the low voltages required to actuate the devices as well as the small area of the mirror reflector. Since the electrostatic contribution to the forces is sufficiently small, they do not need to be considered when modeling the actuation of the devices for deflections larger than 0.1°.

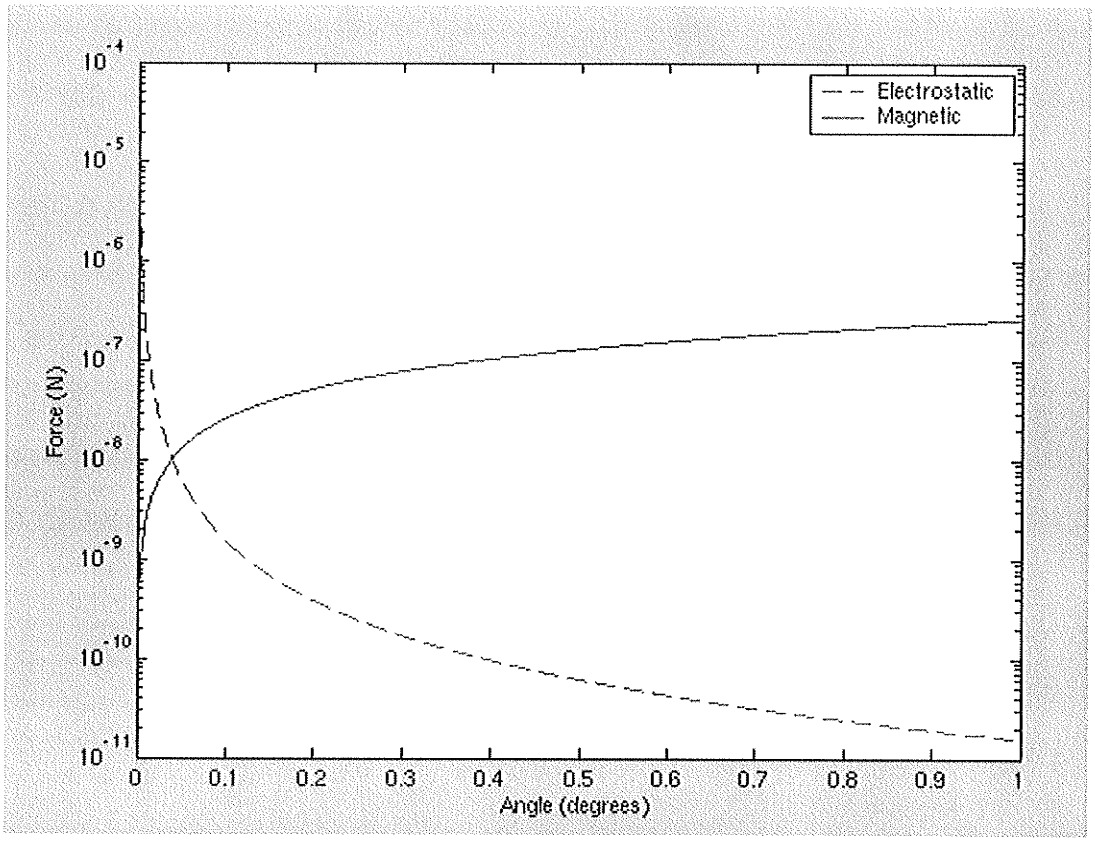

Figure 3-3. Electrostatic and Magnetic force comparison

3.3.2 Thermal and Magnetic Force Comparison

Unlike magnetic and electrostatic forces, thermal forces do not have the same angular dependence. In this section, the thermal and magnetic forces are evaluated at temperatures differences ranging from 0 to 50 degrees. In order to approximate the current through the micro-mirror, (3-11) is evaluated ignoring the contribution from the chrome layer because of the small thickness and much greater resistivity when compared to aluminum.

For small deflections, equations (3-2) and (3-3) may be used to find the displacement, d, at the tip of the micro-mirror structure. However, (3-2) assumes that the temperature is constant over the length of the beam. And so, as a simple approximation, the temperature difference between the hot and cold ends of the flexure arms will be divided by 2 to find the average temperature to be used in (3-2).

$$\Delta T_{average} = \frac{T_{Hot} - T_{Cold}}{2} \tag{3-27}$$

$$R = \frac{(b_A E_A t_A{}^2)^2 + (b_C E_C t_C{}^2)^2 + 2b_A b_C E_A E_C t_A t_C (2t_A{}^2 + 3t_A t_C + 2t_C{}^2)}{6b_A b_C E_A E_C t_A t_C (t_A + t_C)(\alpha_C - \alpha_A)\Delta T_{average}} \tag{3-28}$$

where b_x is the width of the flexure arms, and t_A and t_C is the thickness of the aluminum and chrome respectively. Using beam theory [37], the thermal force at the tip of the structure can be found using

$$F_{thermal} = \frac{3EId}{L_A^{\ 3}} \tag{3-27}$$

The magnet force can be found using the Lorentz force, at a given $I_{thermal}$ and a given angle. The thermal-magnetic force comparison is shown in Figure 3-4. Three plots are shown for the magnetic force. The first for a 5° initial rest angle of the device, and the second for a 45° rest angle, and a 90° rest angle. The magnetic force is the dominant force over the given current range at the different rest angles, and therefore thermal forces may be ignored at low currents and for angles greater than 5°. Thus heat losses by all heat transfer mechanisms can be ignored.

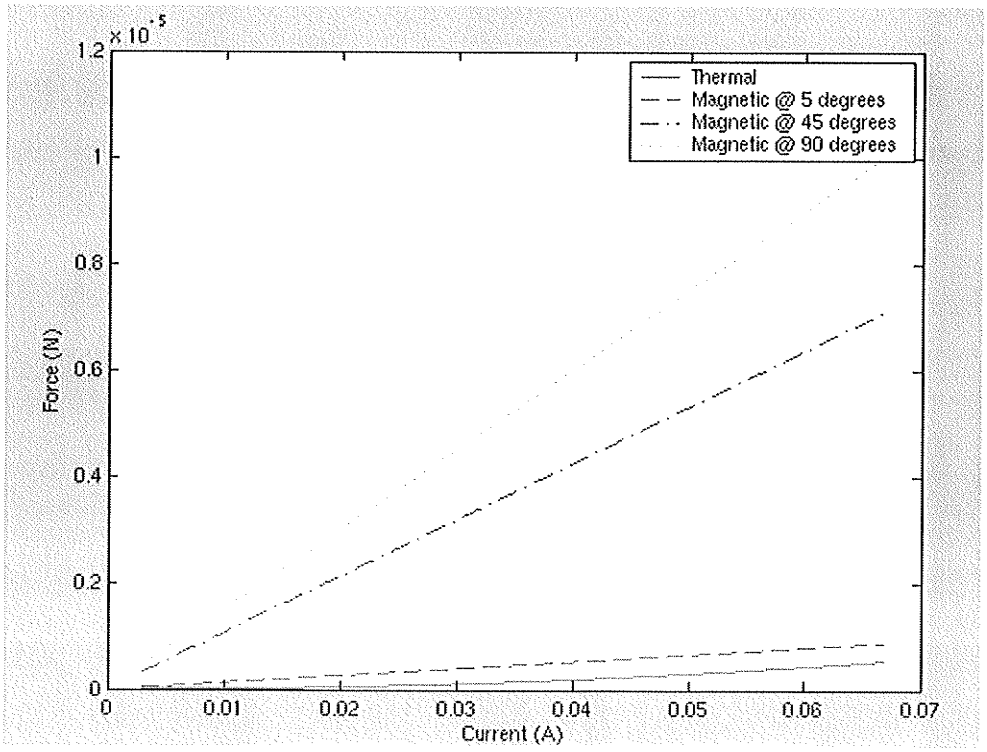

Figure 3-4. Thermal and Magnetic Force Comparison

4. FABRICATION OF MAGNETIC MICRO-MIRROR STRUCTURES

This section will discuss the design development and fabrication of the magnetic micro-mirror structures.

4.1 Patterned and Unpatterned Sacrificial Designs

The basic fabrication procedure begins with a 3" silicon wafer coated with 2 μm of silicon dioxide to act as an electrical insulating layer. Processes steps for the two different fabrication methods performed in this thesis can be seen in Figure 4-1.

A sacrificial material is initially deposited onto the wafer. Depending on the feature size and the amount of sacrificial under-etching, the sacrificial layer can either be patterned (a-g) or remain unpatterned (h-m). In this project, a photoresist sacrificial and silicon sacrificial layer were both attempted. With the sacrificial on the wafer, the metal device layer can than be deposited (b,h). Aluminum was chosen due to the thickness achievable through thermal evaporation as well as its reflective properties. Chrome was chosen since it is known that chrome typically possess tensile stress after deposition by thermal evaporation. The metal layers are then patterned (c,i) with the aluminum mask using lithography. The chrome and aluminum are then etched (d,j) with chrome etch and aluminum etch, respectively. The photoresist mask is subsequently removed. This leaves the wafer with patterned chrome-coated aluminum. Chrome is then patterned (e,k) and etched (f,l) to define the chrome on the

flexures of the actuators. The final step in this fabrication process is the release by etching the sacrificial (g,m).

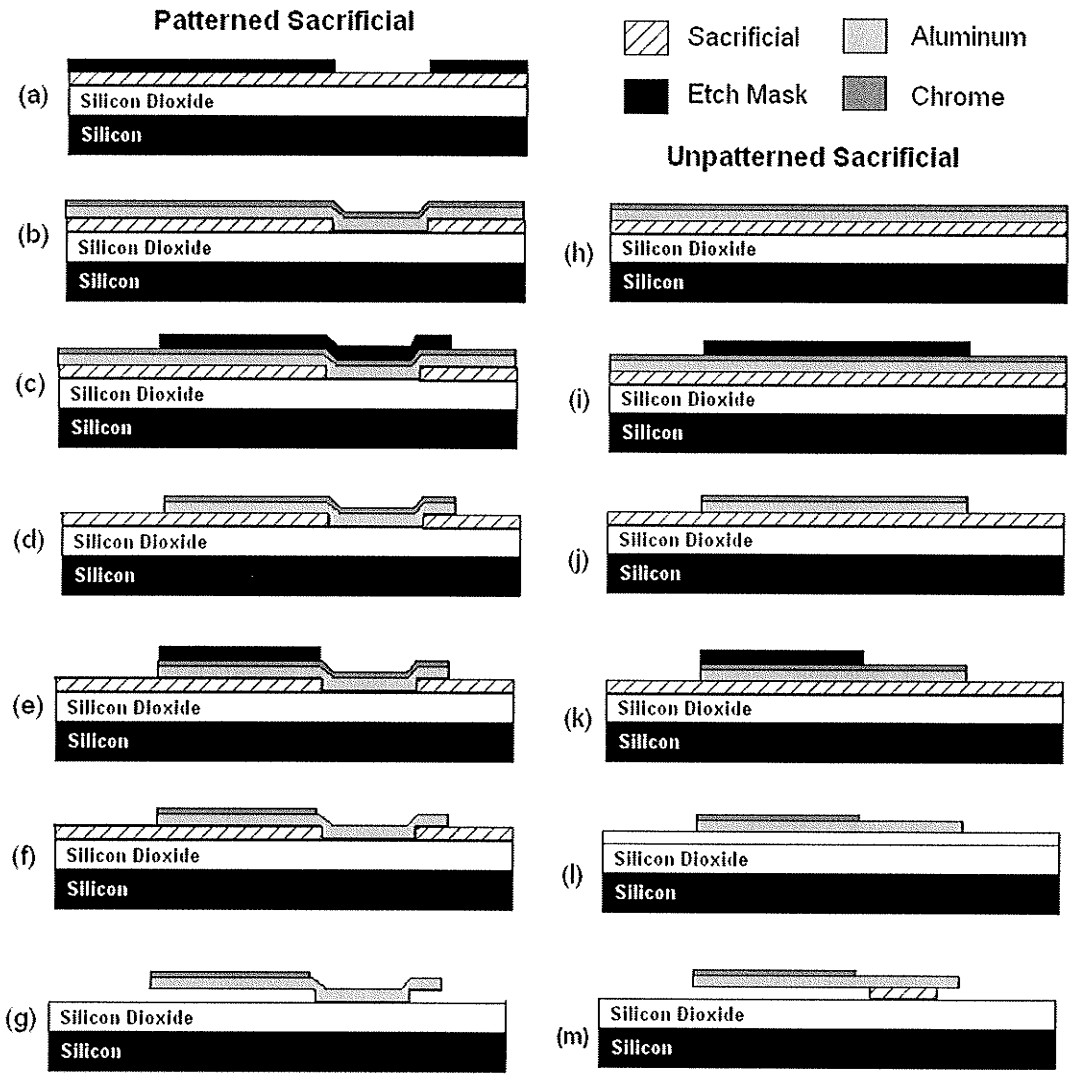

Figure 4-1. Cross-section fabrication process flow

For simplicity, the same aluminum and chrome mask is used for the patterned and unpatterned sacrificial designs. The patterned sacrificial design has the advantage of having a release etch which is not time dependant. Unlike the patterned sacrificial design, if the unpatterned sacrificial is over-etched, the metal anchor pads will completely release from the substrate. In order to prevent the entire structure from releasing from the substrate, the anchor pads which attach the mirror device to the substrate are oversized so they are still anchored to the surface when the mirror structure has released.

Section 4.2 will discuss the fabrication method with a photoresist patterned sacrificial layer. Section 4.3 will discuss the patterned and unpatterned silicon sacrificial layer fabrication method.

4.2 Fabrication with a Photoresist Sacrificial

Photoresist was chosen as a sacrificial layer initially due to its availability, and because there are many processes available to remove the sacrificial layer in order to release the structure. Removal of the photoresist sacrificial was done using two different techniques: plasma etching and wet etching. Photoresist sacrificial removal has adjustable process parameters when using the plasma etcher, while wet etch removal of the photoresist has less process control. Each fabrication process began with a 400um thick silicon wafer with 2μm of oxide. The photoresist chosen for the sacrificial was Olin Hunt HPR 506. Olin Hunt HPRD 419 was the complimenting

developer that is used after exposure. Photoresist spin time was typically set to 35 seconds at 4000 rotations per minute (RPM), which achieved a photoresist thickness of 2μm.

4.2.1 Photoresist Sacrificial Method with Acetone Release

An initial design consisting of simple aluminum bridge structures fabricated over a photoresist sacrificial was investigated. Acetone was used to remove the photoresist. A summary of the process parameters used in this fabrication can be seen in Table 4-1.

Table 4-1. Photoresist Sacrificial Process Parameters with acetone release

Photoresist Spin	4000 RPM (2μm)
Photoresist Soft-bake	60 seconds at 110°C
UV exposure	90 seconds
Photoresist development	30 seconds
Photoresist Hard-bake	20 minute @ 120°C
Thermally evaporated aluminum	0.6μm @ 20 A/sec
Photoresist patterning of aluminum	Standard etch mask parameters Hard bake – 20 minutes
Aluminum Etch	60 second etch @ 50°C
Photoresist Removal	Acetone wet etch

The sacrificial photoresist layer is deposited and patterned lithographically. It was then hard-baked at 120°C for 20 minutes. Aluminum was then thermally evaporated onto the wafer, and patterned with photoresist. When performing the

hardbake when patterning the aluminum device layer, the aluminum device layer began to deform due to outgassing from the photoresist sacrificial below it. This was due to solvent in the photoresist that did not completely evaporate during the initial hardbake of the photoresist sacrificial layer. This solvent expanded during the aluminum patterning hardbake causing visible bubbling (Figure 4-3). These deformations are not acceptable as the deformed flexure arms may cause unpredictable operation.

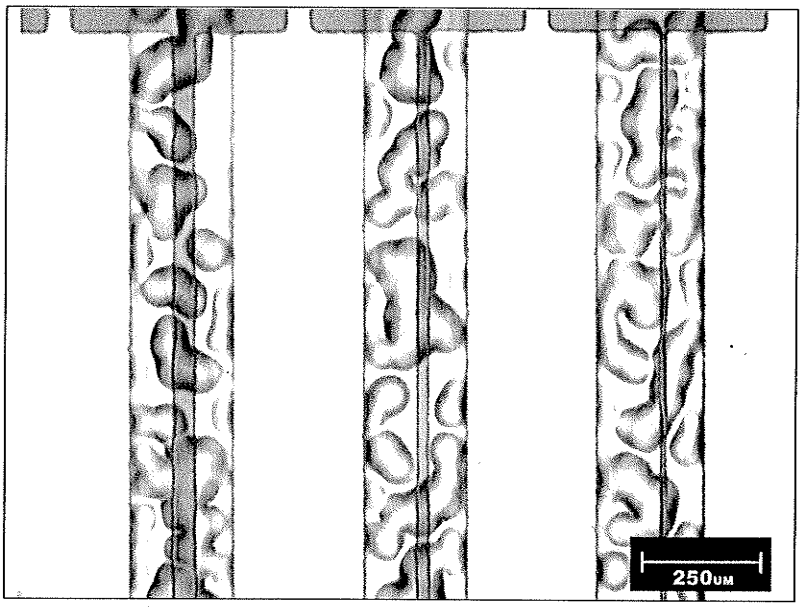

Figure 4-3. Bubbling aluminum due to outgassing of photoresist sacrificial

The aluminum structures were freed by etching the photoresist sacrificial using acetone. Since the acetone is a wet etch, the impact of the liquid acetone on the fabricated devices was enough to destroy or plastically deform many of the structures. Although some devices appeared survive the release process, these devices appeared

to remain adhered to the wafer surface. This is due to liquid surface tension forces that are greater than the restoring forces of the structures. Photoresist residues prevent the devices from releasing after the wafer has dried.

4.2.2 Photoresist Sacrificial Method with Post-Release Processing

A second photoresist removal method was investigated to reduce or eliminate problems with photoresist bubbling and sacrificial release processing. The sacrificial photoresist hard-bake was extended from 20 minutes to 1 hour in order to remove more of the solvent from the photoresist. A summery of the process parameters used in this fabrication can be seen in Table 4-2.

Table 4-2. Photoresist Sacrificial Process Parameters with post-release processing

Photoresist Spin	4000 RPM (2μm)
Photoresist Soft-bake	60 seconds at 110°C
UV exposure	90 seconds
Photoresist development	30 seconds
Photoresist Hard-bake	1 hour
Thermally evaporated aluminum	0.5μm @ 20 A/sec
Photoresist patterning of aluminum	Standard with reduced hardbake Hard bake – 10 minutes
Aluminum Etch	60 second etch @ 50°C
Photoresist Removal	Acetone / Release Process [17]

The sacrificial photoresist was deposited and patterned similar to the initial fabrication. With the increased hard-bake time of the sacrificial layer, the photoresist did not bubble on the following the aluminum deposition and patterning step. The increased hard-bake time however caused the photoresist to crack slightly as can be

seen in Figure 4-4. A 0.5μm aluminum thin-film is then thermally evaporated onto the substrate. The hardbake involved in the patterning of photoresist on the aluminum was also reduced, from 20 to 10 minutes, as bubbling tends to occur at this point during processing because of the heating of the sacrificial.

The aluminum was etched and the photoresist was removed using acetone. A post-release processing step was then done [17]. This step involved placing the devices in a heated bath to reduce stiction following the acetone release. The post-release process involved placing the wafer in a 100°C boiling water bath. Wafers were dried using two different techniques, air dry, and rapid thermal heating using a hot plate. Each had minimal success, with less than 10% of the structures observed to release successfully.

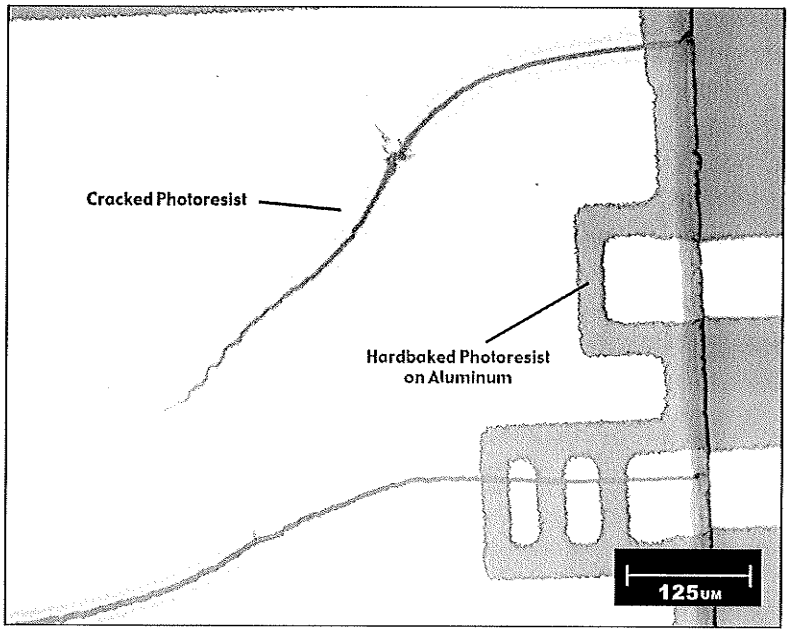

Figure 4-4. Photoresist cracking when hard-bake time was increased to one hour

4.2.3 Photoresist Sacrificial Method with Plasma Release

The third photoresist sacrificial removal method was investigated in order to increase the release yield by using an O_2 plasma etch instead of a wet acetone release. The sacrificial photoresist hard-bake was also reduced from 1 hour to 45 minutes to reduce photoresist cracking. After this reduction in time no cracking was observed, but was long enough to reduce photoresist bubbling seen in first fabrication method. A summery of the process parameters used in this fabrication can be found in Table 4-3.

Table 4-3. Photoresist Sacrificial Process Parameters with plasma release

Photoresist Spin	4000 RPM (2μm)
Photoresist Soft-bake	60 seconds at 110°C
UV exposure	90 seconds
Photoresist development	30 seconds
Photoresist Hard-bake	45 minutes
Thermally evaporated aluminum	0.5μm @ 18 A/sec
Photoresist patterning of aluminum	Standard with reduced hardbake Hard bake – 10 minutes
Aluminum Etch	60 second etch @ 50°C
Photoresist Removal	O_2 Plasma Etch

Oxygen plasma etches are typically used to etch organics, such as photoresist, from the wafer surface[13]. Several recipes were attempted in order to achieve a good lateral etch, since plasma etches tend to be quite vertical. The plasma etch recipe (Table 4-4) used in this fabrication was measured to have a lateral etch rate of

approximately 1μm per minute. These plasma etch parameters were attained by slowly ramping the power and the pressure until the desired etch parameters were achieved. Since many of the features required approximately 50μm of under-etching, the plasma etch is done for 30 minutes since etching occurs at both sides of a feature.

Table 4-4. Sacrificial Photoresist Release Plasma etch parameters

ICP Power	800W
RIE Power	400 W
Pressure	800 mTorr
Etch Time	30 minutes

As with previous fabrications, the photoresist was deposited and patterned to form the sacrificial layer. An intermediate hard-bake time of 45 minutes was chosen to avoid both severe bubbling or cracking of the sacrificial photoresist. Aluminum was then thermally evaporated onto the substrate, which was the subsequently patterned with photoresist. Slight bubbling of the sacrificial photoresist did occur (Figure 4-5), however it did not appear to deform the aluminum layer to any large extent. The aluminum was then wet etched with aluminum etch.

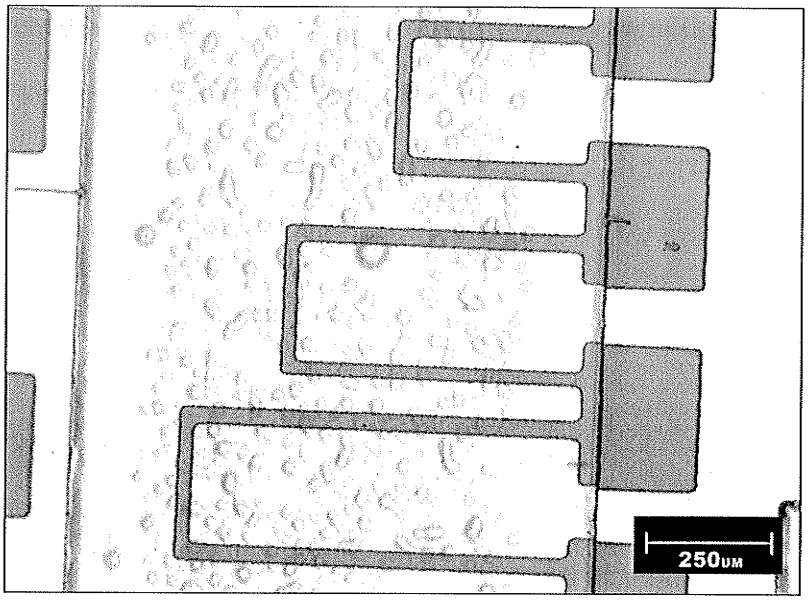

FIGURE 4-5. SLIGHT BUBBLING OF SACRIFICIAL PHOTORESIST DURING THIRD FABRICATION

With the aluminum patterned, the structures were then plasma etched to remove both the aluminum photoresist mask and sacrificial photoresist. The device release yield of the test devices was approximately 10%, however several of the released devices had deformed during release. Small devices designs (15μm features) had the highest occurrence of releasing. Despite the bulk sacrificial photoresist being etched away, a photoresist residue remained which did not allow several of the larger devices to be released (Figure 4-6). Several of the larger devices could be released by pushing the device gently. This is unacceptable in terms of a fabrication process since potentially the wafer could contain thousands of devices.

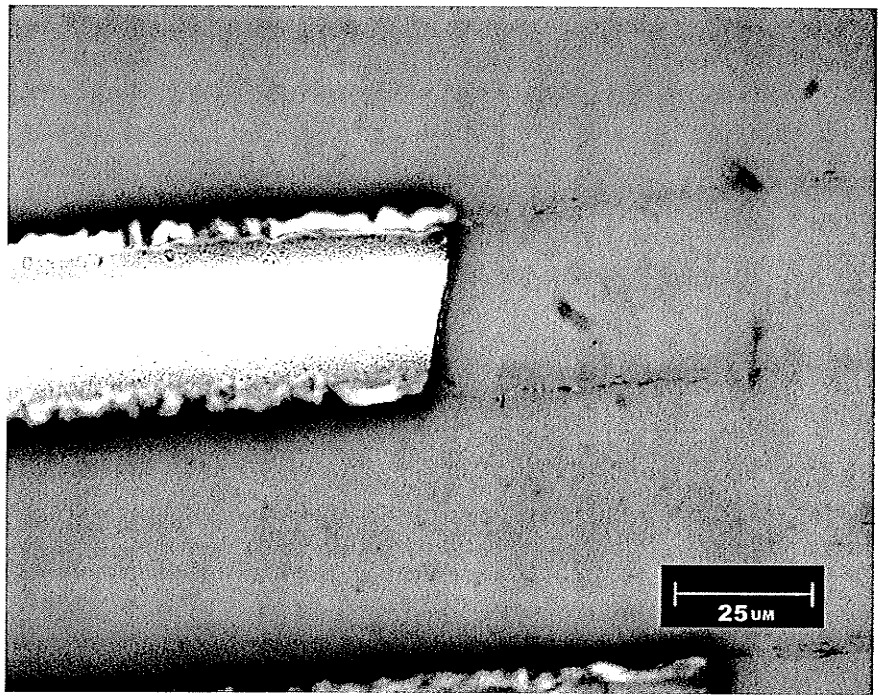

Figure 4-6. Severed beam structure showing photoresist residue

4.2.4 Sidewall Issues with Photoresist Sacrificial

Several observations were taken on other trial fabrication runs not previously mentioned. Olin Hunt HPR 506 photoresist thickness had a range of 1.7μm to 3μm by varying the photoresist spin speed between 2000 RPM and 8000 RPM. The photoresist thickness relative to the thermally evaporated device layer metal (0.1μm-1μm) leads to poor sidewall coverage by the Al metal with the patterned sacrificial designs. Trial fabrications showed that the aluminum metal layer depositions required a thickness of at least 0.5μm in order to remain adhered to the anchor pad after photoresist removal when the sacrificial layer was approximately 2μm.

4.3 Fabrication with Silicon Sacrificial

Due to the poor release yield of the photoresist sacrificial layer and poor sidewall coverage, sputtered silicon sacrificial was used in place of the photoresist. The following section will describe the fabrication procedures involved when using silicon as a sacrificial layer. Some fabrication methods involved patterning the silicon sacrificial layer, while others left the silicon unpatterned.

Similar to the past fabrication processes, the devices were constructed on a 3" oxidized silicon wafer. Sputtering was performed in order to deposit the silicon sacrificial layer onto the wafer. Both DC and RF sputtering experiments occurred at approximately 16 mTorr with a flow rate of approximately 60 standard cubic centimeters per minute of argon. In order to remove the silicon sacrificial, a XeF_2 gas etch was chosen because of its selectivity to etching silicon and low anisotropic etching properties.

4.3.1 Patterned Silicon Sacrificial Method using DC Sputtering

This fabrication method uses a patterned sacrificial design, similar to previous photoresist fabrications. A patterned sacrificial design has the advantage of having a release that does not have time dependence when etching. Table 4-5 shows the process parameter used in this fabrication method.

Table 4-5. Patterned Silicon Sacrificial Process Parameters

Sputtering Power	500 Watts (DC)
Sputtering Time	60 minutes
Silicon Thickness	0.5 μm
Aluminum Thickness	0.6 μm @ 20A/s
Chrome Thickness	0.1 μm @ 5A/s
XeF_2 Etch Time	30 minutes

The silicon is first sputtered onto the wafer surface using DC sputtering. Photoresist is patterned onto the sputtered silicon as an etch mask. The sacrificial silicon was etched using XeF_2 for 30 minutes until it was observed that the exposed silicon had been removed. The photoresist mask was removed using acetone, which left patterned silicon sacrificial on the wafer surface. The aluminum and chrome layers were then deposited by thermal evaporation. They were then patterned and wet etched. The structures were then released by using a XeF_2 etch for 30 minutes.

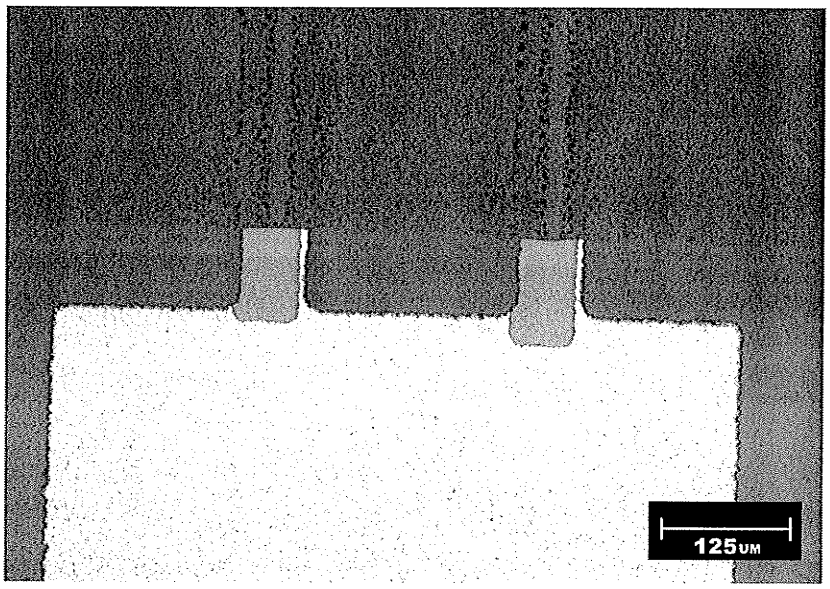

Figure 4-7. Poor Sidewall Coverage of Patterned Silicon Sacrificial

Sidewall coverage with the patterned sacrificial silicon was poor due to the high aspect ratio of the silicon etch. The high aspect ratio does not occur with the photoresist sacrificial since the photoresist reflows during processing, which causes a more gradual step profile. Figure 4-7 demonstrates the structural weakness at the step, where a micro-mirror has been severed from the contact pad during processing. Due to the structural weakness seen at the step, this method was not further investigated. This method may prove successful if a minimal sacrificial thickness is determined which still permits underetching.

4.3.2 Unpatterned Silicon Sacrificial Method using DC Sputtering

This fabrication method using silicon is slightly different than previous fabrications since it uses an unpatterned sacrificial. The sacrificial layer can remain unpatterned since the released structure is significantly smaller than the contact pads that attach the actuators to the wafer surface. This eliminates the problems associated with sidewall coverage since all the metal layers lie in the same plane during fabrication. Table 4-6 describes the process parameters for the unpatterned silicon sacrificial fabrication.

Table 4-6. Initial Silicon Sacrificial Process Parameters

Sputtering Power	500 Watts (DC)
Sputtering Time	90 minutes
Silicon Thickness	0.6-0.7 μm
Aluminum Thickness	0.7 μm
Chrome Thickness	0.15 μm
XeF_2 Etch Time	30 minutes

The silicon is first sputtered onto the wafer surface using DC sputtering. The aluminum and chrome layers were deposited by thermal evaporation. They were then patterned and wet etched. Figure 4-7 shows some of the devices before releasing in XeF_2 showing the different dimensions investigated. The sacrificial silicon was etched using XeF_2 using the quick-pulse method for 25 minutes; with a nitrogen purge cycle 7 pulses to remove any reactants possibly adhering to the wafer surface. This fabrication method had good device release success (Figure 4-8), however none of the structures that had no chrome on the flexures released. The chrome on the flexures lifts the structure up providing improved underetching.

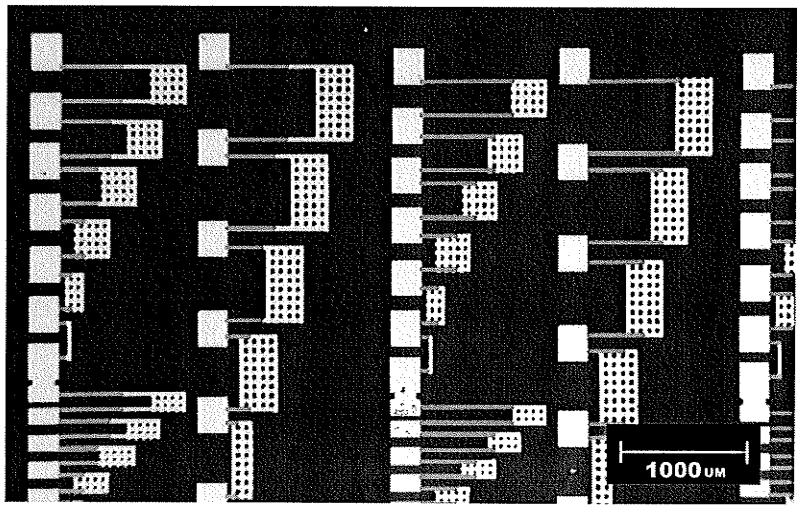

Figure 4-7. DC Sputtered Silicon sacrificial devices before release

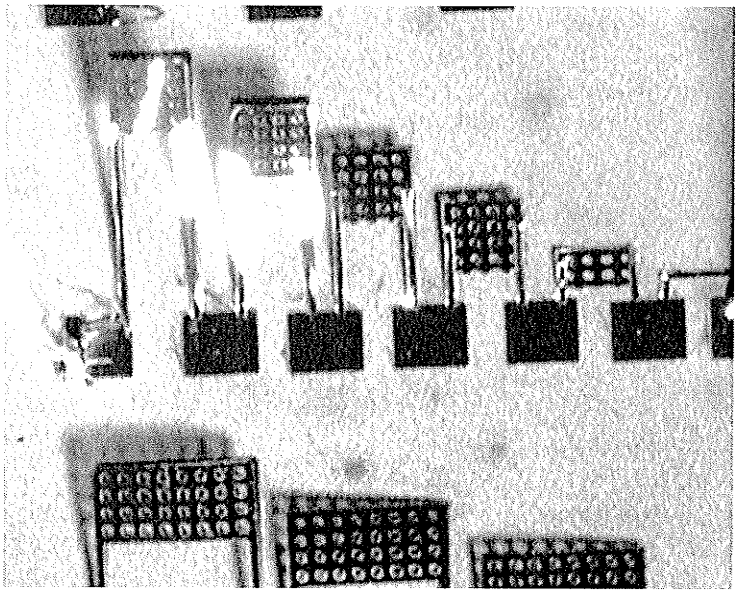

Figure 4-8. DC Sputtered silicon sacrificial after release

4.3.3 Unpatterned Silicon Sacrificial Method using RF Sputtering

The deposition rate of silicon appeared to decrease between different DC sputtering runs, which was due to oxidation of the silicon target. Therefore subsequent sputter depositions were performed with an RF target bias instead of DC bias in order to achieve a more consistent sputter rate. Details of the fabrication test using this method are as follows:

Table 4-7. Unpatterned Silicon Sacrificial Process Parameters using RF Sputtering

Sputtering Power	400 Watts (RF)
Sputtering Time	20 minutes
Silicon Thickness	0.5 μm
Aluminum Thickness	0.4 μm
Chrome Thickness	0.10 μm
XeF_2 Etch Time	35 minutes

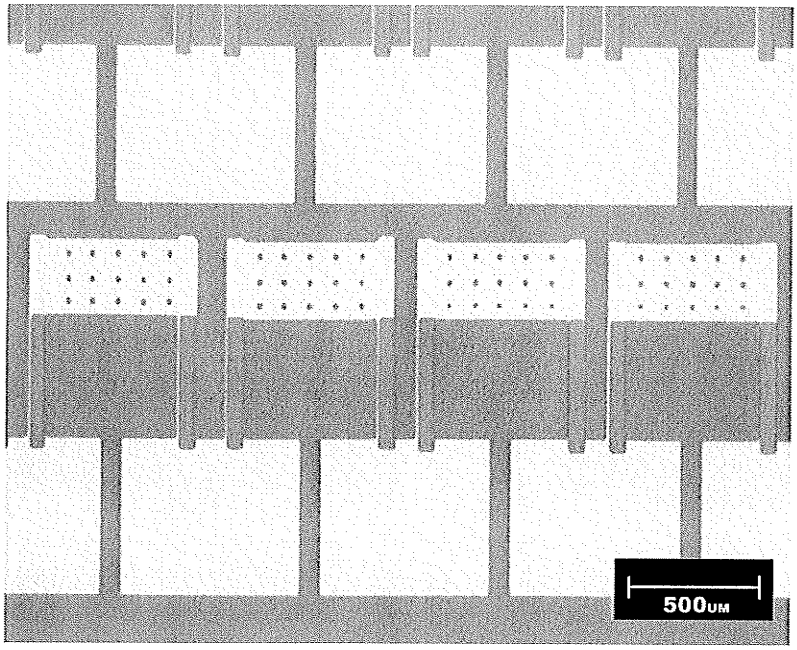

Figure 4-9. RF Sputtered silicon sacrificial micro-mirrors before release

At 400 watts, the sputtering rate of silicon was approximately 25nm/min. The aluminum and chrome thin films were deposited using thermal evaporation similar to previous fabrications. Figure 4-9 shows an array of fabricated devices before release using the RF silicon sacrificial method. Many of the structures successfully released in the XeF_2 system, however because of XeF_2 loading some of the smaller devices at the center of the wafer did not release. There was no noticeable difference between the etch rates of the DC sputtered silicon and the RF sputtered silicon using XeF_2, each taking approximately 25 minutes before the micro-mirrors would begin releasing. Except in locations where it was discovered that the silicon sacrificial was incompletely etched away, this technique appeared to be 95% successful. Figure 4-10 shows several released micro-mirrors which were fabricated in an array.

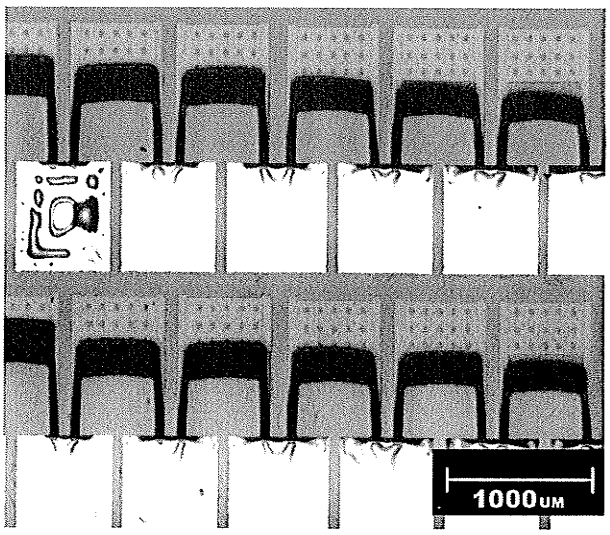

Figure 4-10. RF Sputtered silicon sacrificial micro-mirrors after release

The devices appear black in color due to the angular position of the micro-mirrors which do not reflect the light back into the microscope. The variation in the lift angle of the micro-mirrors in this array will be addressed in the following chapter.

5. FABRICATION ANALYSIS OF STRESSED MAGNETIC MICROMIRRORS

This chapter further investigates the fabrication of the micro-mirrors using the silicon sacrificial. Observations and images were obtained with an Olympus microscope and probe station (Figure 5-1).

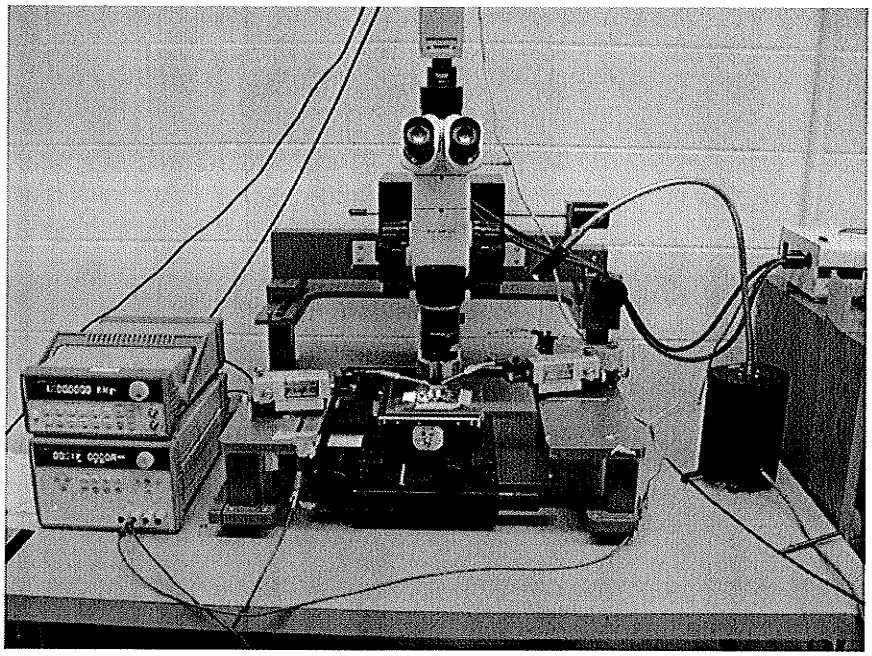

Figure 5-1. Probe station in the Nanosystems Test Lab at the University of Manitoba

Wafers were initially placed in a plastic Petri dish, however this induced charge into wafer that did not allow them to be tested. Testing and storing the silicon wafer within a metal container overcame this obstacle.

5.1 Silicon Sacrificial Gas Loading Problem with XeF_2

The silicon sacrificial release process was a significant improvement over the photoresist sacrificial, however problems still existed with the process. The etch time in the XeF_2 etch system is crucial, since the sacrificial remains unpatterned to eliminate any sidewall coverage problems. Given enough time all devices will theoretically release, since the contact pads that adhere the devices to the wafer will also release. Etching is stopped when it observed the contact pads were starting to etch. However, the XeF_2 vapor does not etch the wafer in a uniform manner. Due to gas loading and the chamber configuration, etching is non-uniform. The perimeter of the wafer tends to etch first; therefore the middle of the wafer remains relatively underetched. Due to this effect, many of the devices in the middle of the wafer are not released when the devices on the edge of the wafer have completed their release. Plasma etching tends to be more uniform over the wafer surface, however the high vertical anisotropy of plasma etching makes the lateral underetch of the devices difficult.

5.2 Silicon Sacrificial Residues

The silicon sacrificial fabrication method has a tendency to leave thin silicon residues after etching with XeF_2. This residue appeared with both RF and DC sputtered silicon sacrificials. The precise cause of the residual silicon is unclear, and is beyond the scope of this thesis. Photoresist sacrificial residue tends to outline the structures, whereas the silicon sacrificial residue tends to be present on the sacrificial

silicon where it is not covered with a patterned metal structure (Figure 5-2). This residual silicon cannot be etched further due to the unpatterned sacrificial design, which would underetch the contact pads which keep the structures on the wafer. The location of the silicon residue would suggest that some chemicals during the wet etch of aluminum and chrome may inhibit the silicon etch. This is supported by fact that the sacrificial silicon under the

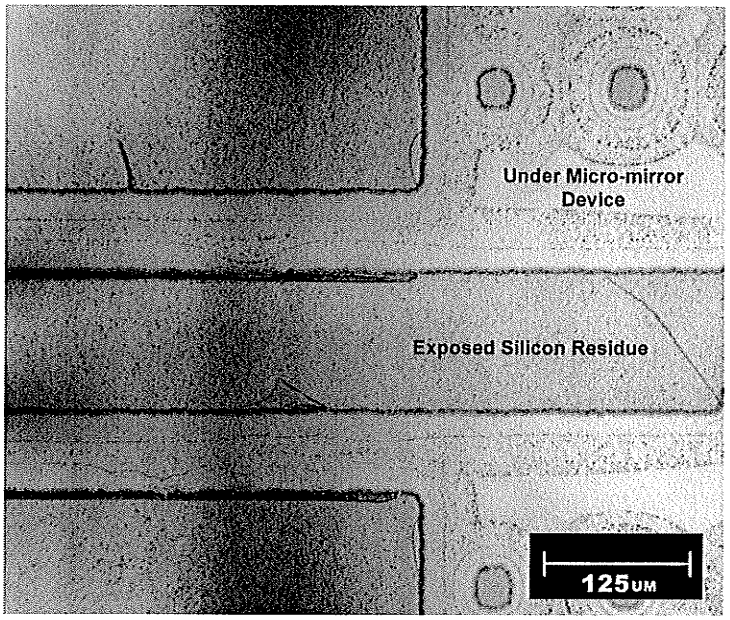

Figure 5-2. Residue present where not covered by aluminum

released structures, which is not exposed to these chemicals, is etched completely to the oxide on the wafer. This remaining silicon did not appear to affect the performance of the micro-mirrors, however may have prevented some micromirrors from releasing due to residue at the perimeter of the devices. Figure 5-3 demonstrates how unanchored aluminum test beams do not release from the wafer surface without the presence of the chrome layer. Eliminating this residue needs to be further

investigated. Some success has been reported using a carbon tetrafluoride (CF_4) plasma etch to etch the bulk exposed sacrificial silicon and then using XeF_2 to etch the silicon under the micromirrors [38].

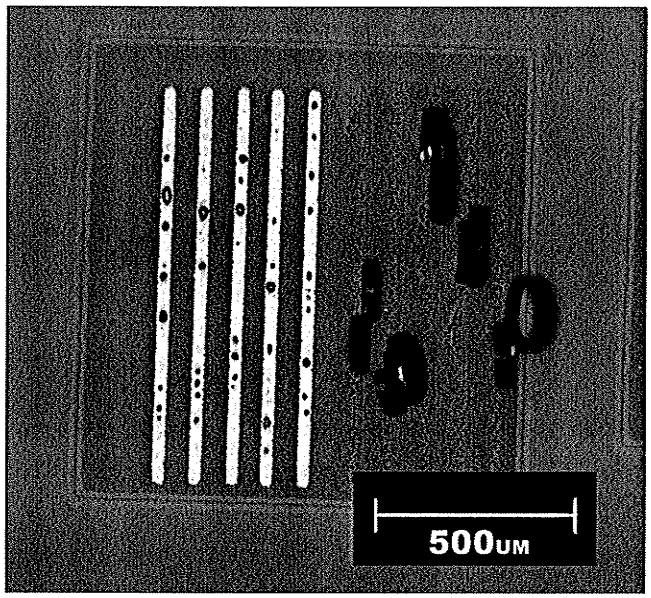

Figure 5-3. Unanchored aluminum test beams on silicon sacrifical which do not release without chrome (left), and which release when coated with chrome (right)

5.3 Chrome Length and Rest Angle

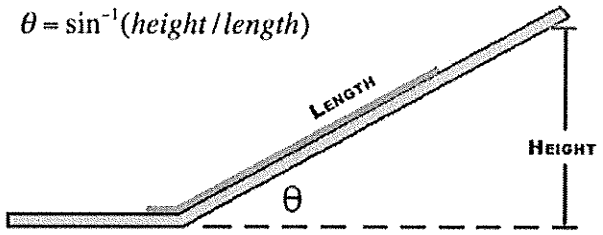

Figure 5-4. Rest angle schematic

The initial rest angle of several micromirrors was calculated by measuring the difference between the base of the actuator and the end of the released structure using an Olympus microscope (Figure 5-4). This is done prior to actuating the devices, since plastic deformation may occur with excessive angular deflection. The height was measured by a focusing technique with the microscope, which involves measuring the difference between two focus points using the microscope dial. This technique is accurate to +/-5μm with a 20x objective, due to hysteresis of the microscope dial and error associated with human focusing. The flexure arms are approximated to be flat despite the stress from the bimetallic layer. The curvature may be seen by placing the micromirrors at 90° and observing any bow in the flexure arms (Figure 5-5). Table 5-1 describes the specifications of the devices under test for angle measurements.

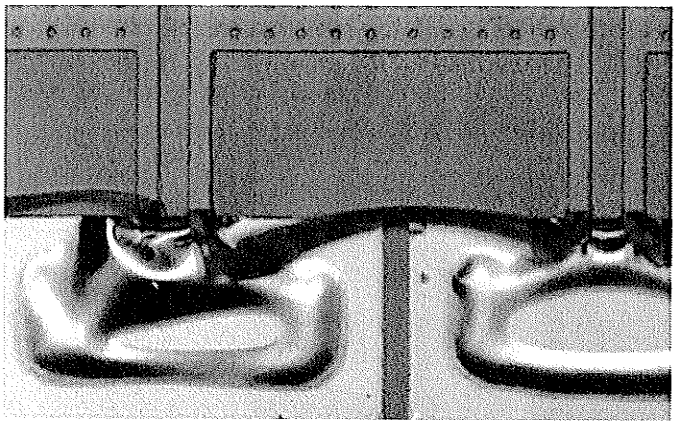

Figure 5-5. Micromirror positioned at 90° to observe curvature in flexure arms

Table 5-1. Specifications of devices used in Rest Angle Measurements

Sacrificial Method	1μm RF Si
Aluminum Thickness t_A	0.5μm
Chrome Thickness t_C	100nm
Flexure Width W_A	28μm
Reflector Width W_R	300μm
Reflector Length L_R	280um
Flexure Length L_A	100 – 1000μm
Chrome Length L_C	0 – 1000μm

Figure 5-6 shows the change in angle with respect to the beam length, and chrome length percentage along the flexure arms. The actuators initial rest angle increases with the flexure arm length, as well as percentage of chrome on the flexure arms.

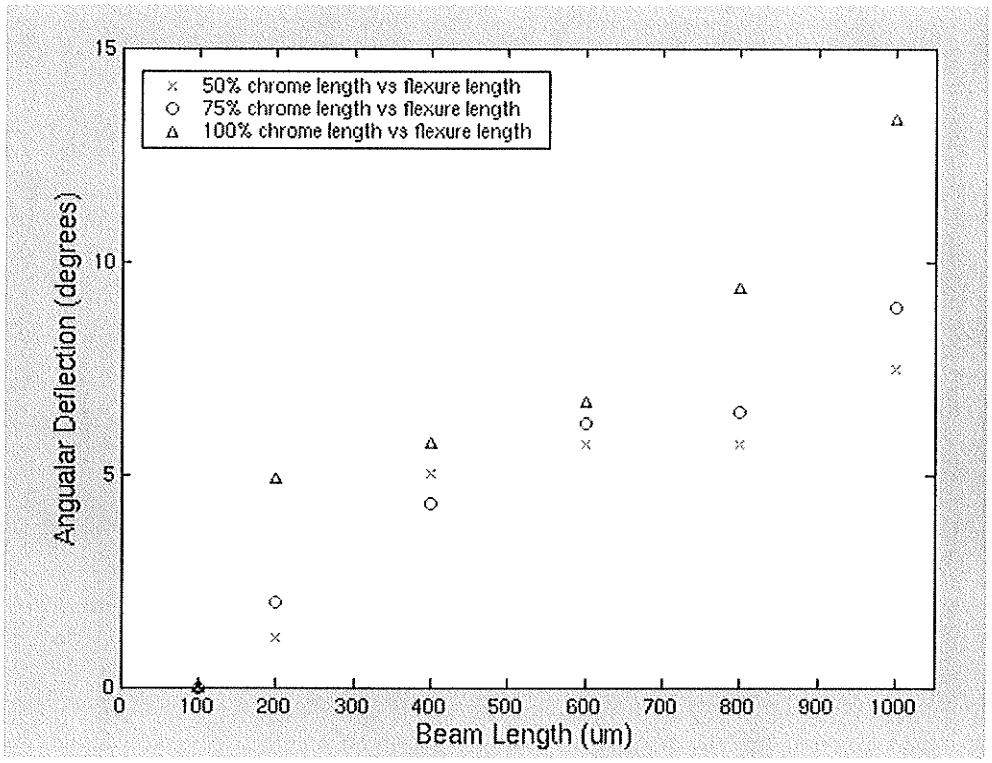

Figure 5-6. Angular Deflection due to Initial Stress (300x280μm reflector)

This test shows that adjusting the amount of chrome on the flexure arm can set the initial rest angle. Greater process control in film deposition is required in order to have a predictable initial rest angle, as the film stress tends to be quite sensitive process parameters such as deposition rate and temperature.

5.4 Fabrication Consistency

A large number of identical structures were fabricated into arrays on the same silicon wafer to better understand the variability of the silicon fabrication methods. All the devices are exposed to similar conditions since they are fabricated on the same

silicon wafer. Variation in the characteristics of the actuators may be due to several factors, such as film thickness, mask irregularities, and non-uniform etching.

5.4.1 Fabrication Consistency Design

The elements of the array were chosen based on release success and initial release angle observed from previous fabrications. Four designs were fabricated based on the 800μmx600μm micro-mirror with full chrome length. Figure 5-7 demonstrates four designs (A-D) that were configured into arrays for the fabrication analysis.

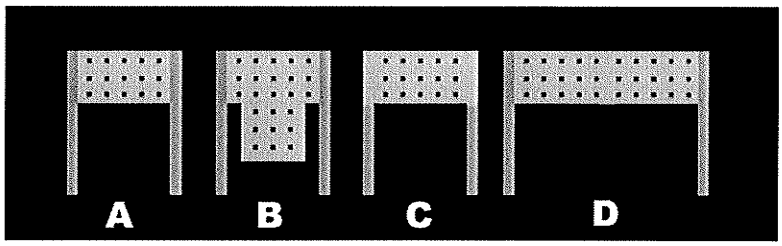

Figure 5-7. Schematics of four magnetic microactuators composed of aluminum (silver) and chrome (brown)

Design A is the simple micro-mirror structure that has shown promising results from previous experiments. Design B is a perturbation on design A, where the reflective surface has been enlarged to give the structure more reflective surface area. Design C contains the same structural properties as design A, however the chrome length has been reduced so that it does not impinge on the reflective end of the actuator. Design D also has similar structural properties to design A, however the width of the actuator has been doubled.

The 800μmx600μm actuators (A,B,C) were configured into 10x4 arrays, whereas the 1200μmx600μm actuator (D) was placed in a 6x4 array due to size restrictions of the wafer. Additionally, all four designs were scaled in two separate ways: 125% in length and 125% in both length and width. The scaled actuators were produced primarily for release analysis and not for actuation.

5.4.2 Fabrication Process of Micro-mirror Arrays

The micro-mirror arrays were constructed on the same 3" oxidized silicon wafer. Table 5-2 describes the parameters and fabrication details used to construct the devices.

Table 5-2. Geometric Design Parameters of the Stressed Magnetic Actuators

Sacrificial Method	1μm RF Si @ 16mTorr
Aluminum Thickness t_A	0.5μm @ 20A/s
Chrome Thickness t_C	100nm @ 5A/s
Flexure Width W_A	56μm
Reflector Width W_R	600-1200μm
Flexure Length L_A	100 – 1000μm
Chrome Length L_C	0 – 1000μm
Reflector Length L_R	300-800um

Silicon sacrificial is first sputtered onto the wafer for 30 minutes at 400 Watts for a sacrificial thickness of one micron. The aluminum and chrome layers were deposited by thermal evaporation, patterned and then etched. The XeF_2 Quick-Pulse method was used to etch the sacrificial silicon. A dehydration bake was performed for

10 minutes at 120°C as recommend by Brazzle et al. in [39] to prevent HF formation and reduce any moisture found on the wafer surface. This significantly increased the etch rate of the initial pulses, however the etch rate decreased during succeeding pulses. The etch chamber was purged with nitrogen every 5 pulses (10 minutes) in order to attempt to remove the reactants away from the wafer surface. This proved successful as the etch rate noticeably increased on the following pulses. The etch was stopped when a number of contact pads were observed to have been significantly underetched.

5.4.3 Design Compatibility with Fabrication

Each micro-mirror design responds differently to the fabrication process largely due to the differences in geometry. The similarities of the elements in each array allows for observations on the design response to the fabrication process. Figure 5-8 shows a sample of the four micro-mirror designs after they have been released.

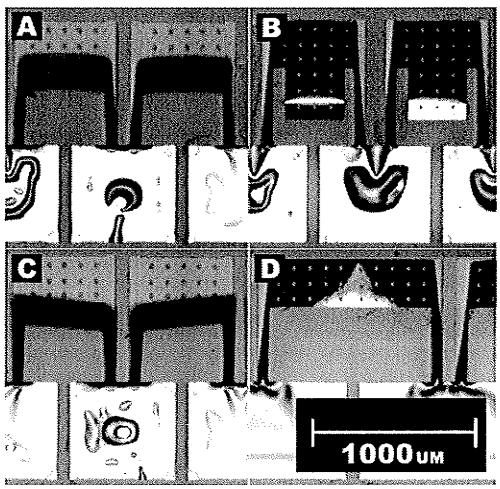

Figure 5-8. Examples of 4 micro-reflector array designs after release

Design A and C both released with minimal defects and an initial rest angle between 15 and 65 degrees. Design B and D tended to have smaller release angle between 1 and 10 degrees. This lower release angle may be attributed to the stressed flexure arms not capable of lifting the entire structure. The flexure arms of designs B and D also tend to curl inward due to stress and a portion of the micro-mirror still fixed onto the wafer surface. The rest angle of the micro-mirrors is not only dependent on the flexure arms, but also the overall geometry of the micro-mirror.

5.4.4 Initial Rest Angle Variation

The initial height of all the micro-mirrors was measured and recorded using a microscope focusing technique. The angle can then be calculated using trigonometry described in section 5.3. Table 5-3 shows the average initial rest angle is obtained from each of the design sets, as well as the standard deviation of each set.

Table 5-3. Average and Maximum Initial Rest Angles of 4 micro-mirror arrays

	# of Devices	Base Size		Scaled Length 125%		All Scaled 125%	
		μ	σ	μ	σ	μ	σ
Design A	40	26.7°	15.2°	32.4°	13.2°	38.5°	9.9°
Design B	40	3.9°	2.3°	3.4°	0.4°	3.5°	0.7°
Design C	40	47.0°	6.0°	39.7°	16.9°	52.4°	8.5°
Design D	24	7.5°	13.9°	5.8°	10.4°	7.0°	10.6°

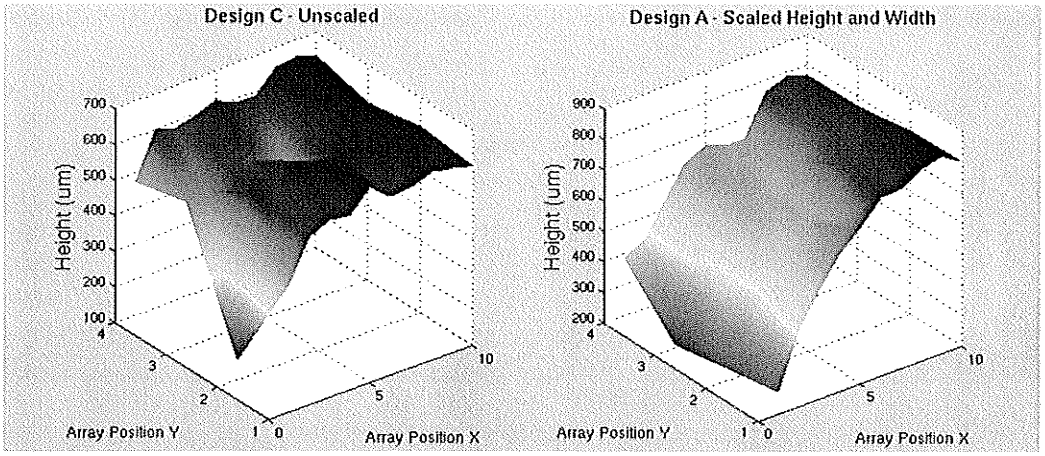

Figure 5-9. Example of Initial Rest Height variation of two micro-mirror arrays

The initial rest angle data (Table 5-3) demonstrates the variability in the fabrication process. An example of the variation observed across the arrays can be seen in Figure 5-9. The elements in the array tend to have similar properties to neighboring elements, which would suggest the micro-mirror initial rest angle is dependant on the location on the wafer. This location dependence comes from the variability in the film thickness and XeF_2 etching. Film thickness of the chrome and aluminum was measured at three points (Figure 5-10) on the wafer using an Alpha-Step profilometer (Table 5-4). Film thickness variation of less than 5% would suggest that the large variation comes from the silicon and XeF_2 etching.

Table 5-4. Film Thickness Variation over the Wafer Surface

	Left	**Middle**	**Bottom**
Aluminum Thickness	0.510μm	0.502μm	0.498μm
Chrome Thickness	0.104μm	0.103μm	0.101μm

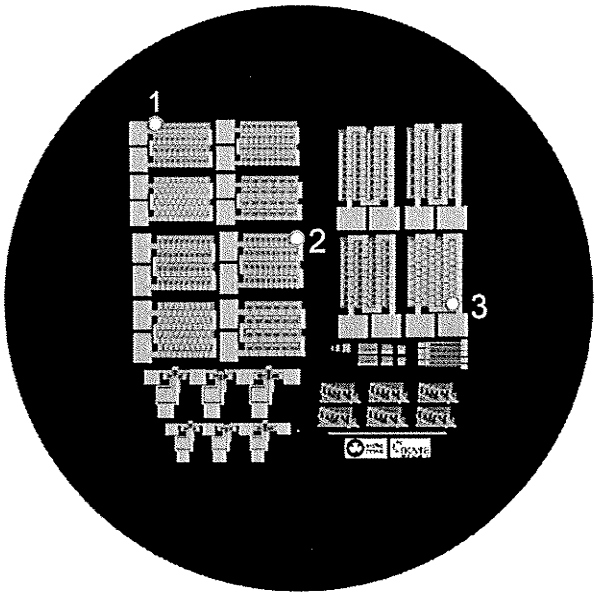

Figure 5-10. Three Points Measured to Determine Thickness Variation on Wafer

5.5 Issues with an Unpatterned Silicon Sacrificial Layer

The fabrication step that appeared to cause the largest variation in devices characteristics is the XeF_2 release process. Problems arise from the non-uniform etching with an unpatterned sacrificial layer. This unpatterned sacrificial method is used to overcome problems associated with step coverage when using a patterned sacrificial that creates structural weakness at the step. Non-uniform etching occurs due to the configuration of the XeF_2 etch chamber and loading. The unpatterned sacrificial and the non-uniform etching caused the contact pads to underetch dissimilarly, which can be seen to some extent in Figure 5-11. The location of the actuators on the wafer surface was therefore a factor to the release and characteristics of each actuator.

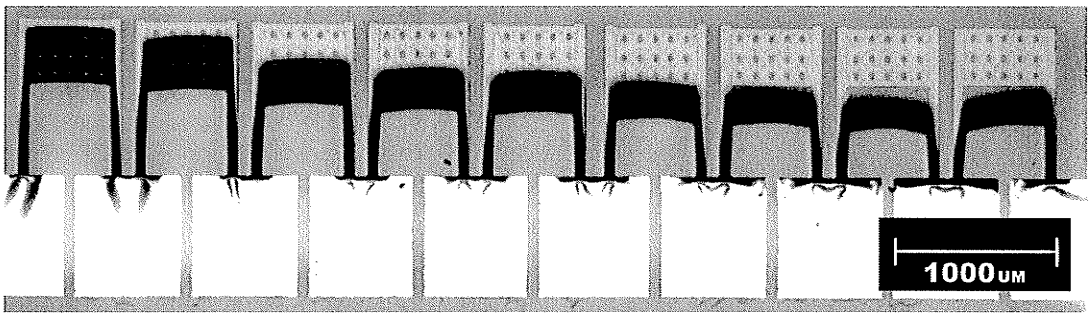

Figure 5-11. Unpatterned sacrificial etching causing variability in initial rest angle

The edge of the contact pad where the flexure is attached must support the deflected micro-mirror in order to maintain a particular angle. When the contact pads are over-etched there is a tendency for the micro-mirror to set at a lower rest angle. In some cases the contact pad will lift up where it connects to the flexure arms due to the over-etching, combined with the weight of the micro-mirror and the stress in the

flexure arm. Lifting of the contact pad can be seen on the furthest left micro-mirror in Figure 5-8, where the contact pad surface appears to be bubbled near the flexure arm.

A patterned thin silicon sacrificial design may eliminate both the problems associated with step coverage and etching under the contact pad. The sacrificial film should be kept sufficiently thin to minimize step coverage issues, while the patterned sacrificial design would eliminate any contact pad under-etch.

6.TESTING AND MODEL VERIFICATION OF MAGNETIC MICRO-MIRRORS

This chapter discusses the actuation of the micro-mirrors using different stimuli. Thermal and magnetic response of the micro-mirrors is investigated. The model for actuation of the micro-mirrors is also verified. Lifetime and frequency testing is performed to better comprehend where the micro-mirrors may be applied towards. Table 6-1 describes the fabrication process used for the micro-mirrors under test. A schematic of the micro-mirrors can be seen in Figure 6-1.

Table 6-1. Design Parameters of the Actuated Micro-mirrors

Sacrificial Method	1μm RF Si
Aluminum Thickness t_A	0.5μm
Chrome Thickness t_C	100nm
Flexure Width W_A	28,56μm
Reflector Width W_R	600-1200μm
Flexure Length L_A	100 – 1000μm
Chrome Length L_C	0 – 1000μm
Reflector Length L_R	300-800um

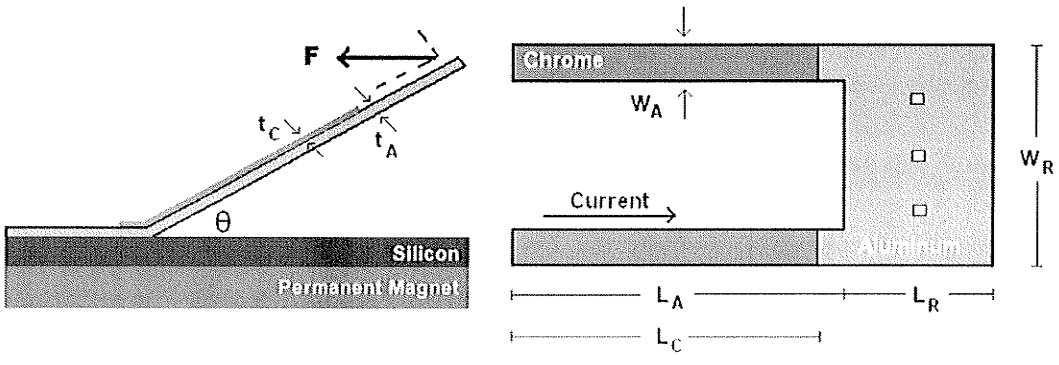

Figure 6-1. Schematic of micro-mirrors under test

6.1 Current Driven Failure

The micro-mirror structure has limits as to the amount of current before the device will fail due to thermal heating. The micro-mirror structure tends to fail at the flexure arms, due to their high resistance and small surface area for cooling. The failure current is therefore dependent on the geometry of flexure arms, primarily width and thickness. Flexure widths of 28μm and 56μm are used in the design of the micro-mirrors. Five micro-mirrors of each flexure width were tested in order to observe when this failure occurs. Current through the micro-mirrors is slowly increased until the flexures fail. The maximum and minimum values are recorded for each flexure arm width after several tests are performed (Table 6-2).

Table 6-2. Maximum and Minimum Currents before flexure failure

	28μm	**56μm**
Minimum Current	96mA	114mA
Maximum Current	108mA	131mA

In order to not drive future experiments into failure, these maximum and minimum currents are taken into account. Micro-mirrors are not tested within a 15mA range of the minimum failure value.

6.2 Transition Angle

When the micro-mirror undergoes large angular deflections, the flexure arms may transition from the elastic to the plastic regime. The angle at which this occurs is dependant on geometry and material properties:

$$\theta_{elastic-plastic} = \frac{\sigma_y w_m t_m^{\,2} L_m}{4 E_m I_m} \tag{2-5}$$

The transition angle of the bimetallic flexures may be estimated by substituting the geometrical parameters, and by using a weighted average of yield strength (σ_{Al} = 124MPa, σ_{Cr} = 1GPa) using the material thickness [40, 41]. The calculated transition angle for the fabricated micro-mirrors was 37.8 degrees. The micro-mirrors were observed to plastically deform at approximately 40 degrees.

6.3 Thermal Response

The thermal response of the micro-mirrors was tested in order to confirm the modeling in section 3.3.2, that stated that motion due to thermal expansion may be neglected. Thermal actuation is measured by removing the permanent magnet from the test setup. This eliminates any Lorentz forces that may move the micro-mirror in the presence of the magnetic field. Current is driven through the micro-mirrors in

order to increase the temperature of the bimetallic flexures. Figure 6-2 shows a micro-mirror undergoing thermal testing from 0mA to 75mA.

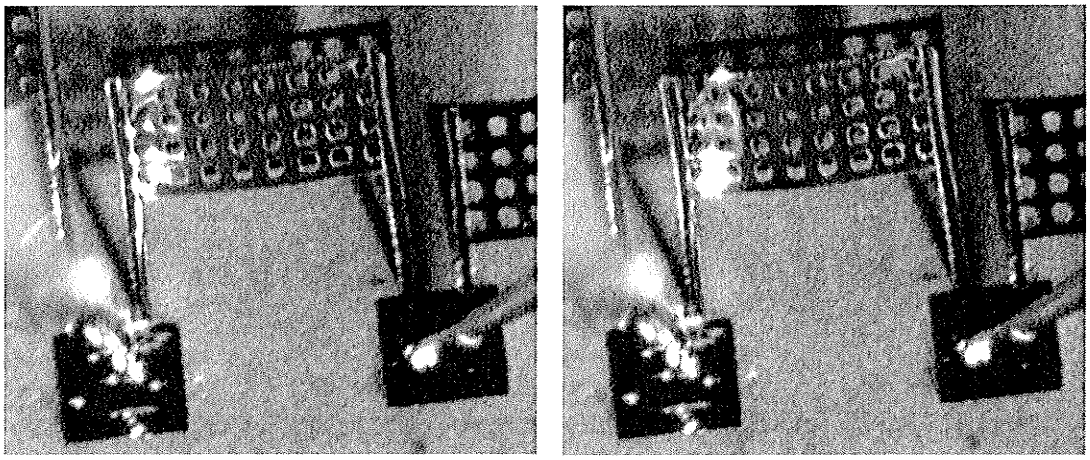

Figure 6-2. Thermal testing of micro-mirrors at 0mA (a) and 75mA (b) which deflected approximately 5mA

Thermal expansion in the bimetallic flexure arms caused the micro-mirror to move vertically approximately 5 degrees. Simulations of the angular displacement of the beam (Figure 6-3) would suggest the micro-mirror would move close to 8 degrees, however the equation tends to deviate when the radius of curvature is less than the length of the beam. The radius of curvature is equal to the length of the beam at approximately 55mA (or 4 degrees). Heating also causes the reflecting pad to expand slightly. This expansion of the reflecting pad towards the flexure increases the curvature of the reflecting pad as it pushes outwards.

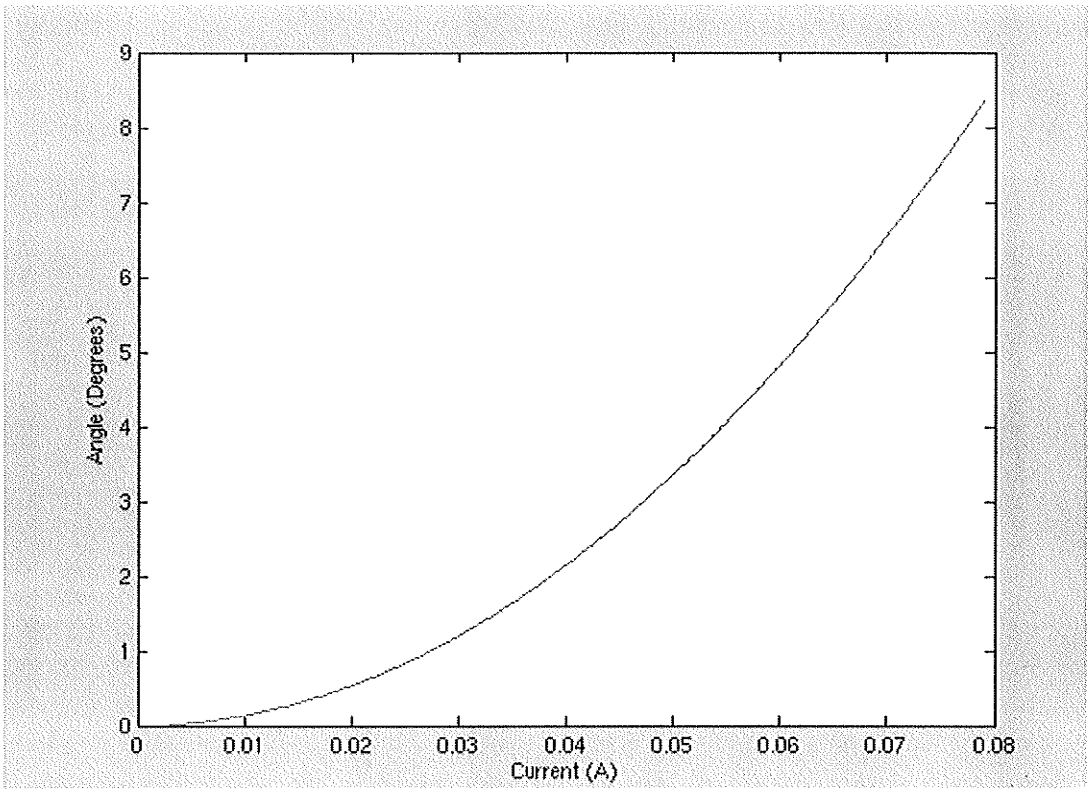

Figure 6-3. Simulation showing the projected angular deflection due to thermal heating

6.4 Magnetic Response

A permanent magnet is placed under the wafer in order to measure the magnetic response of the micro-mirrors when a current is applied. Two permanent magnets of different magnetic field strength are used to determine the deflection range of each magnet. Micro-mirrors of various sizes are also tested. Deflection is measured using a microscope focusing technique, explained in Section 5.3.

6.4.1 Deflection Range

Two permanent magnets were placed directly under the wafer during testing: a cylindrical magnet and hard drive magnet. Using a Bell 610 Gaussmeter, the magnetic field on top of the silicon wafer is measured for each magnet. The magnetic field of the cylindrical magnet was 0.035 Teslas. The magnetic field of a hard drive magnet was 0.25 Teslas.

Using a fiber light, the structures are tested as micro-mirrors by actuating the devices a small distance by applying current through the micro-mirror (Figure 6-4). Current was increased in 25mA steps, and the deflection was recorded. Results from testing the 800μm x 600μm micro-mirror are presented in Table 6-3. These results show that a smaller magnetic field is capable of deflection angles similar to what is used in various light modulation applications, such as the Bell Labs LambdaRouter [21] and Texas Instrument DLP chip [22]. Deflection angles greater than 90 degrees can be achieved by implementing a larger magnetic field source, such as the hard drive magnet.

Table 6-3. 800μmx600μm Magnetic Micro-mirror (800μm chrome length) with 28μm flexure and 250μm reflector

Magnet Source	Magnetic Field	0mA	25mA	50mA	75mA
Cylindrical	0.035 T	10°	15°	24°	34°
Hard Drive	0.25 T	10°	46°	70°	110°

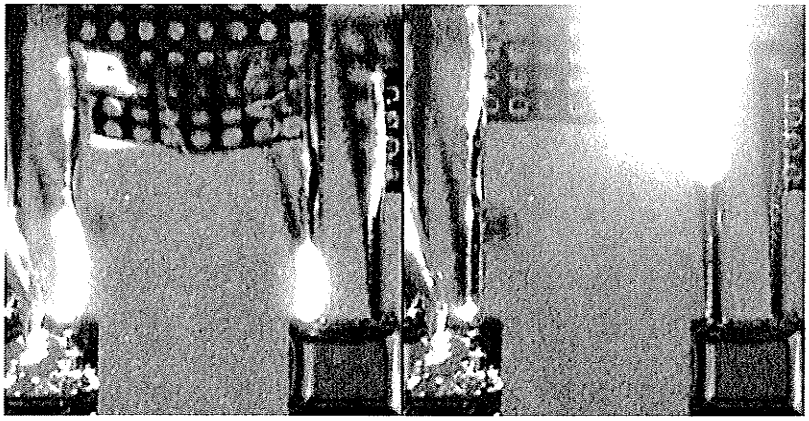

Figure 6-4. Magnetic Actuation of 800μm x 600μm micro-mirror

The reflecting pad tends to bend slightly under large Lorentz forces since the thin metal film is quite flexible. In order to reduce this flexibility the width of the reflecting pad must be reduced, or a rigid material such as SiO_2 or Si_3N_4 is required under the reflective aluminum thin film.

6.4.2 Different Geometries

Three different geometries are tested to see how the micro-mirror design will respond to the Lorentz forces (Table 6-4). A smaller current is used than in previous experiments in order to avoid deforming the flexures during actuation. The hard drive magnet (0.25 Teslas) is used to achieve large deflections with minimal current. Results of these measurements can be seen in Table 6-5 and Figure 6-5.

Table 6-4. Dimensions of the micro-mirrors under test (56μm Flexure widths, 300μm Reflector Length)

Micro-mirrors	**1**	**2**	**3**
Flexure Length	800μm	800μm	1000μm
Reflector Width	600μm	1200μm	750μm

Table 6-5. Angular deflection vs. applied current

Current (mA)	**800x600μm (angle)**	**800x1200μm (angle)**
Initial	69.33	90.00
2.50	72.19	101.12
5.00	74.65	110.86
7.50	78.46	120.29
10.00	82.56	127.46
12.50	85.28	133.03
15.00	90.00	137.88
17.50	93.37	141.84
20.00	97.44	146.18
22.50	101.54	149.36
25.00	105.35	152.89

Current (mA)	**1000x750μm (angle)**
Initial	79.76
2.00	84.90
4.00	87.45
6.00	90
8.00	93.56
10.00	96.38
12.00	100.24
14.00	102.84
16.00	105.47
18.00	108.13
20.00	112.47
22.00	117.53
24.00	122.23

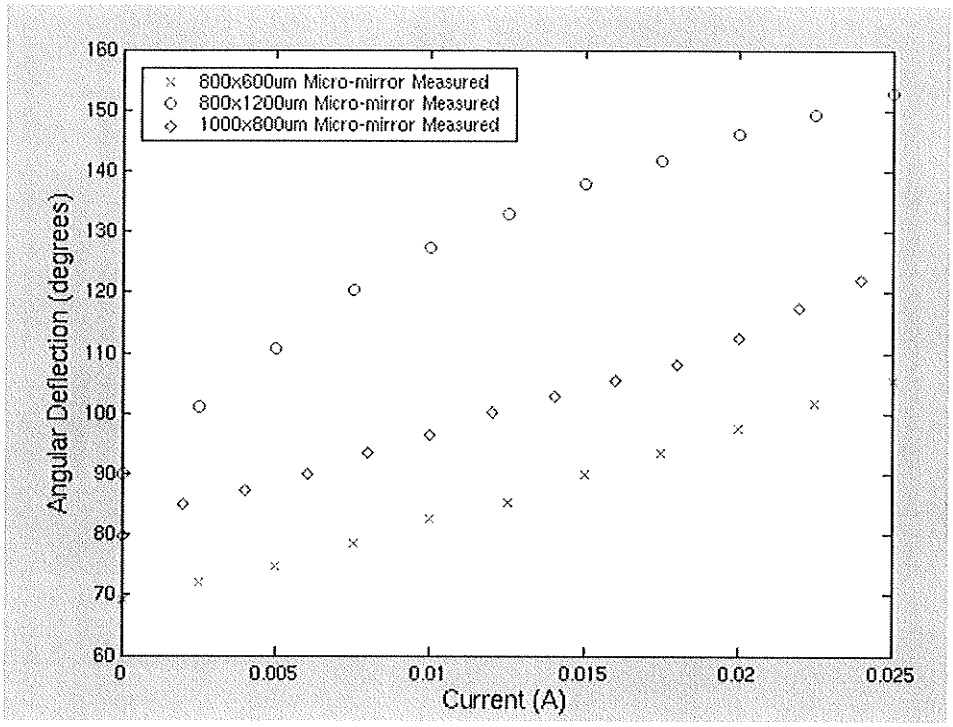

Figure 6-5. Angular deflection versus Current of Micro-mirrors with different geometry

6.5 Model Verification of Magnetic Micro-mirror

The micro-mirrors deflection may be approximated using the angular displacement model (3-19) described in Chapter 3. Design parameters (Table 6-1), bulk material properties (Table 3-2), and the initial rest angle are substituted into the model and the function is iterated.

$$\theta_x = \frac{(IW_R B)(L_A)(\sin\theta_{x-1})L_m}{E_m I_m} + \theta_{x-1} \tag{3-19}$$

Since the bending region of the actuator consisted of both aluminum and chrome, a weighted average of the Young's modulus (E_m, E_{Cr}=140GPa, E_{Al}=70GPa,) [35, 36] is taken using the film thickness (0.5μm Aluminum, 0.1μm Chrome) as a quick approximation. The bending length of the flexures (L_m) was observed to be between 30μm and 50μm, therefore a nominal value of 40μm is used for modeling. In order to approximate the angle of the micromirror, the flexures and micromirror are assumed to flat as in previous experiments. Some curvature to the flexures and micromirror may occur due to the stressed bimetallic structure, however for many of the structures this appears to be minimal.

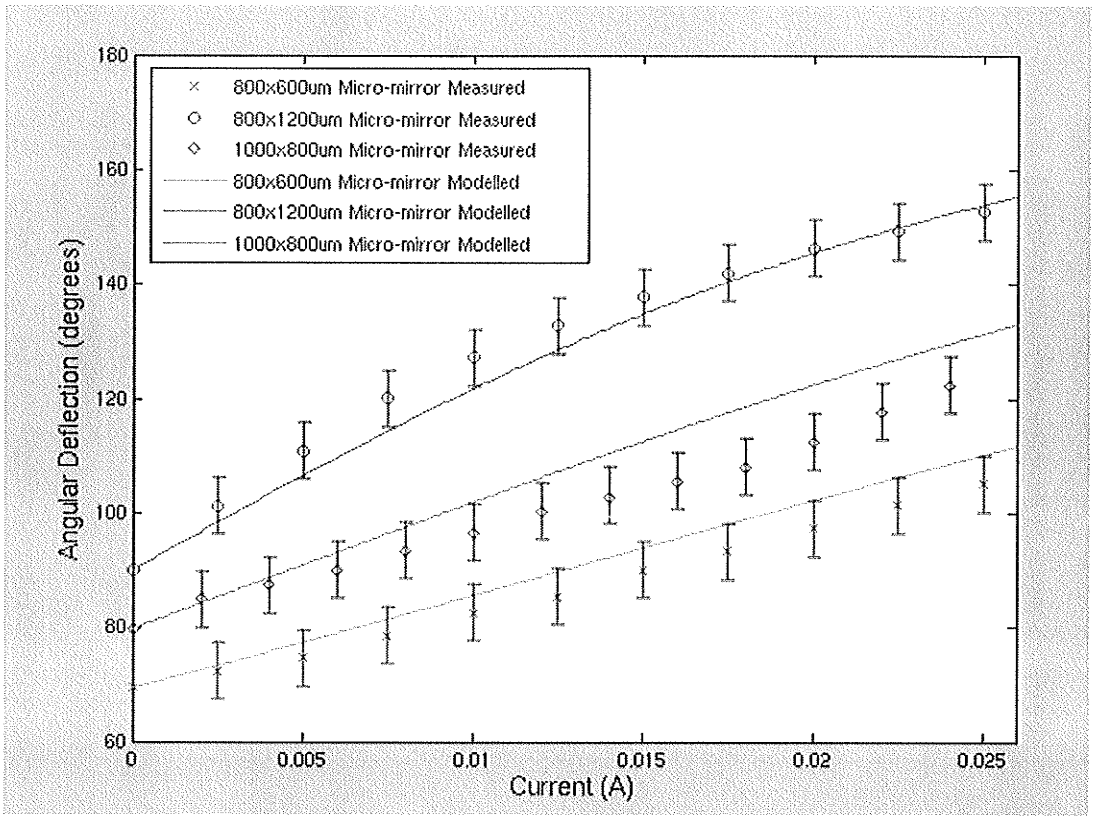

Figure 6-6. Measured and Theoretical angular displacement of three fabricated designs

The angular displacement model for the stressed magnetic actuators appears to have fair agreement with the measured data as a first order approximation (Figure 6-6). The majority of the calculated deflections fall within a 5 degrees error tolerance of the measured deflections. Variability in the material thickness and etching during the fabrication process may account for the mismatch between the measured and theoretical actuation distance. Additional variability may come from the slight curvature in the flexure arms, variation in the bending length, as well as some delaminating of the contact pad due to underetching.

6.6 Frequency Testing

Frequency response of the micro-mirrors is an important characteristic to understand in order to specify future applications for the devices. The response of the micromirrors was optically measured by using a Motorola MRD500 photodiode in the probe station microscope eyepiece. The photodiode, which has nanosecond response time, was chosen to measure the response since the CCD camera (Sony SSC-DC50A) and human eye have difficulty observing frequencies larger than 30Hz. The change in intensity from the micro-mirrors was observed on a digital oscilloscope by measuring the optically induced voltage across the photodiode. This measured voltage gives the relative angular deflection of the micro-mirror, however this voltage is non-linear due to the properties of the photodiode. Therefore the actual deflection distance is not known. A fiber light is positioned to reflect off the micromirror and onto the photodiode in the eyepiece. All additional light sources in the test environment were turned off to eliminate external sources from affecting the test results. The test setup and a schematic of the test apparatus can be seen in Figure 6-7.

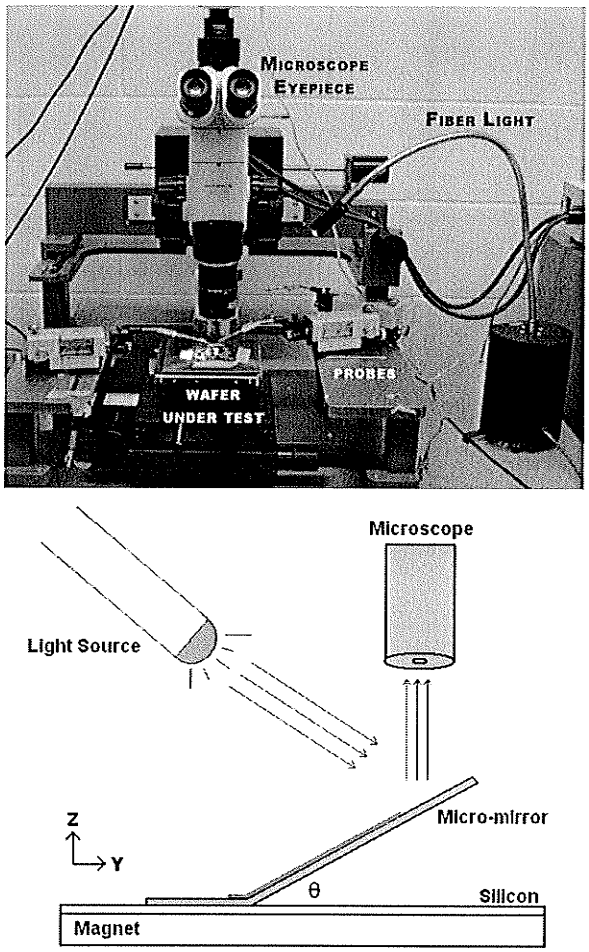

Figure 6-7. Probe Station and Equipment used for frequency testing

The 1000x800μm micro-mirrors were initially actuated between 45 and 60 degrees (100mV sinusoid, 100mV offset, 0.25T magnetic field) at low frequencies. The mirrors initial position is chosen such that there is little reflection when micromirror is not actuating, and more light reflected during deflection.

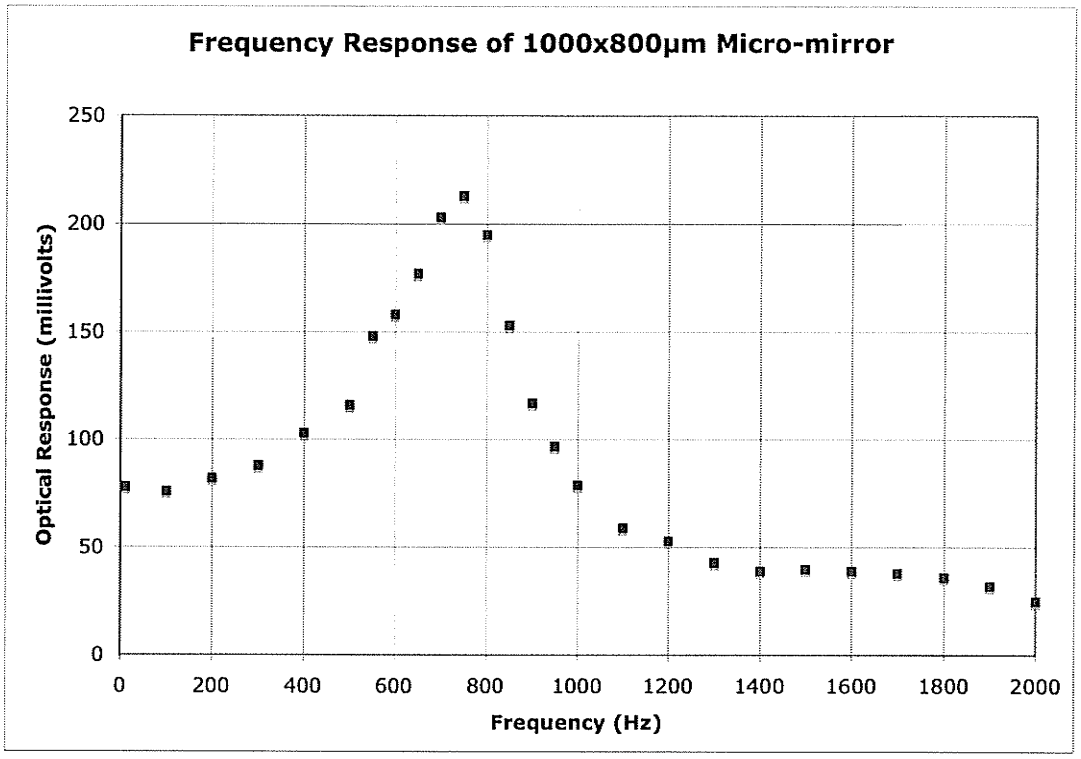

Figure 6-8. Measured Frequency Response of Magnetic Micro-mirrors using MRD500 Photodiode

Under the same excitation, the frequencies were swept from 1 to 2000 Hz and the high and low response to the photodiode was recorded. The difference between the high and low response recorded can be seen in Figure 6-8.

The actuation distance remains fairly constant up to 300 Hz, whereupon the deflection distance increases and peaks at 780 Hz. At frequencies greater than 780Hz, the actuation distance quickly decays.

6.7 Micromirror Lifetime

An AC signal was applied to several micro-reflector arrays to test their lifetime and deflection drift. The lifetime of the devices typically depends on number of cycles and the deflection distance. Cycle tests were performed by applying a 100 Hz signal to the micro-reflector arrays. When operating the micro-reflectors in the elastic regime the structure lifetime is significantly greater than when operating in the plastic regime. Elastic deflections of 30 degrees have been shown to actuate greater than 2 million cycles with little variation in deflection distance. The micro-mirror was not tested beyond 2 million cycles, however because of no noticeable change in deflection, they should be able to sustain many more cycles. Plastic deflections larger than 90 degrees have been shown to only have a lifetime of a few thousand cycles. These micromirrors that failed tended to break in the bending regime of the flexure near the contact pad.

7. CONCLUSION

7.1 Summary

In conclusion, an out-of-plane micromachined magnetic force actuator was designed and successfully fabricated into a micro-mirror structure. A simple and affordable fabrication process was developed using microfabrication technology. Several different stressed magnetic actuators are fabricated in order to determine a suitable design for the fabrication process. A model is formulated to predict the angular motion of the actuators. Preliminary testing shows that large actuation distances can be achieved with small currents. The stressed magnetic actuators were implemented in a micro-mirror array to explore the variability in the fabrication process. Advantages of the design and fabrication process include large actuation distances, small number of masks and materials. The main disadvantage of the fabrication process is the variability in underetching of contact pads, however this is a tradeoff to avoid problems with step coverage. Further refinement of the fabrication process and design are required to optimize the performance of the micro-mirrors.

7.2 Future Work and Recommendations

The scaling of this technology would reduce power requirements as well as reduce real estate on the wafer surface. Therefore, an optimal size should further be determined depending on the application of the micro-mirrors. Fabrication with a patterned silicon sacrificial layer should also be explored, however the sacrificial

thickness needs to be sufficiently small to avoid poor sidewall coverage issues. Due to complexity of the geometry of these devices when released, a finite element model should be developed in order to improve simulated results. Some investigation should go into providing the reflector with a more rigid surface or low stress film so that it may be more uniform. Many other MEMS applications may exist for these actuators, and therefore new uses should be explored.

BIBLIOGRAPHY

1. G.T.A. Kovacs, *Micromachined Tranducers Sourcebook*. 1998, New York, New York: McGraw-Hill Companies. 911.
2. H. Baltes, et al. "IC MEMS microtransducers" in *International Electron Devices Meeting*. San Francisco, CA. 1996.
3. M. Cohn, et al. "MEMS Packaging on a budget (fiscal and thermal)" in *9th International Conference on Electronics, Circuits and Systems*. 2002.
4. P. Koeneman, I. Busch-Vishniac, and K. Wood, "Feasibility of Micro Power Supplies for MEMS". *Journal of Microelectromechanical Systems*, 6(4): p. 355-362. 1997.
5. S.J. Fiedziuszko. "Applications of MEMS in communications satellites" in *13th International Conference on Microwaves, Radar, and Wireless Communications*. 2000.
6. G.M. Rebeiz, G.-L. Tan, and J.S. Hayden, *RF MEMS Phase Shifters: Design and Applications*, in *IEEE Microwave magazine*. 2002. p. 72-81.
7. B.P. Gogoi and D. Mladenovic. "Integration technology for MEMS automotive sensors" in *IEEE 2002 28th Annnual Conference on the Industrial Electronics Society (IECON 02)*. 2002.
8. R.E. Sulouff. "Silicon sensors for automotive applications" in *International Conference on Solid-State Sensors and Actuators*. San Francisco, CA. 1991.
9. M. Ruan, J. Shen, and C.B. Wheeler, "Latching microelectromagnetic relays". *Sensors and Actuators A*, 91: p. 346-350. 2001.
10. J.W. Choi, et al., "New magnetic bead-based, filterless bio-separator with planer electromangetic surfaces for integrated bio-detection systems". *Sensors and Actuators B*, 68: p. 34-39. 2000.
11. C.H. Ahn, Y.J. Kim, and M.G. Allen, "A planar variable reluctance magnetic micromotor with fully integrated stator and coils". *Journal of Microelectromechanical Systems*, 2(4): p. 165-173. 1993.
12. W.R. Grove, "Philos. Trans. Faraday Soc." 87. 1852.
13. S.A. Campbell, *The Science and Engineering of Microelectronic Fabrication*. 2nd ed. 2001, New York: Oxford University Press Inc. 603.
14. K. Williams, K. Gupta, and M. Wasilik, "Etch Rates for Micromachining Processing - Part II". *Journal of Microelectromechanical Systems*, 12(6): p. 761-778. 2003.
15. B. Bahreyni and C. Shafai. "Deep Etching of Silicon with xenon difluoride gas" in *IEEE CCECE*. Winnipeg, Manitoba. 2002.
16. K. Walsh, J. Norvill, and Y. Tai. "Photoresist as a Sacrificial Layer by Dissolution in Acetone" in *14th IEEE International Conference on Microelectromechanical Systems*. Interlaken Switzerland. 2001.
17. T. Abe, W. Messner, and M. Reed, "Effects of Elevated Temperature Treatments in Microstructure Release Procedures". *Journal of Microelectromechanical Systems*, 4(2): p. 66-75. 1995.
18. M. Bartek and R. Wolffenbuttel, "Dry release of metal structures in oxygen plasma: process characterization and optimization". *Journal of Micromech. Microeng.*, 8: p. 91-94. 1998.

19. L. Lin, E.L. Goldstein, and R.W. Tkach, "Free-Space Micromachined Optical Switches with Submillisecond Switching Time for Large-Scale Optical Crossconnects". *IEEE Photonics Tecnology Letters*, 10(4): p. 525-527. 1998.
20. O. Cugat, et al., "Deformable Magnetic mirror for adaptive optics: technological aspects". *Sensors and Actuators A*, 89: p. 1-9. 2001.
21. L.J. Hornbeck, *Digital Light Processing(tm): A New MEMS-Based Display Technology. A Document.*
22. D.J. Bishop, C.R. Giles, and G.P. Austin, "The Lucent LambdaRouter: MEMS technology of the future here today". *IEEE Communicatinos Magazine*, 40(3): p. 75-59. 2002.
23. C.H. Ji, Y.K. Kim, and B.K. Choi. "Design and fabrication of electromagnetic micromirror with bulk silicon mirror plate and aluminum spring" in *IEEE/LEOS International Conference on Optical MEMS*. Kauai, HI. 2000.
24. M.A. Michalicek, J.H. Comtois, and C.C. Barren. "Design and charcterization of next generation micromirros fabricated in a four-level, planarized surface-micromachined polycrystalline silicon process" in *Second Annual IEEE International Conference on Innovative Systems in Silicon*. Austin, TX. 1997.
25. H. Toshiyoshi, D. Miyauchi, and H. Fujita, "Electromagnetic Torsion Mirros for Self-Aligned Fiber-Optic Crossconnectors by Silicon Micromachining". *IEEE Journal of Selected Topics in Quantom Electronics*, 5(1): p. 10-17. 1999.
26. D. Horsley, et al., "Optical and Mechanical Performance of a Novel Magnetically Actuated MEMS-Based Optical Switch". *Journal of Microelectromechanical Systems*, 14(2): p. 274-284. 2005.
27. I. Shimoyama, O. Kano, and H. Miura. "3-D Micro-structures Folded by Lorentz Force" in *Eleventh Annual International Workshop on Microelectromechanical Systems*. Heidelberg, Germany. 1998.
28. I. Shimoyama, H. Miura, and R. Holzer. "Lorentz force actuation of flexible thin-film aluminum microstructures" in *IEEE International Conference on Intelligent Robots and Systems 'Human Robot Interaction and Cooperative Robots'*. Pittsburgh, PA, USA. 1995.
29. M. Schiffer, V. Lalble, and E. Obermier. "Design and Fabrication of 2-D Lorentz Force Actuated Micromirrors" in *IEEE/LEOS Internation Conference on Optical MEMS*. 2002.
30. A. Baba, et al. "2 Axes Optical Switch with Holding Mechanism" in *16th IEEE International Conference on Micro Electro Mechanical Systems*. 2003.
31. J.S. Ko, "Development and Application of a Laterally Driven Electromagnetic Microactuator". *Applied Physics Letters*, 81(3): p. 547-549. 2002.
32. J. Haji-Babaei, C.Y. Kwok, and R.S. Huang. "Integrable Active Microvalve with surface micromachined curled-up actuator" in *1997 International Conference on Solid-State Sensors and Actuators*. Chicago, IL. 1997.
33. C. Chang and P. chang, "Innovative micromachined microwave switch with very low insertion loss". *Sensors and Actuators A*, 79: p. 71-75. 2000.
34. J. Zou, et al., "Plastic Deformation Magnetic Assembly (PDMA) of Out-of-Plane Microstructures: Technology and Application". *Journal of Microelectromechanical Systems*. 2001.

35. S. Senturia, *Microsystem Design*. 2001, Norwell, Massachusetts: Kluwer Academic Publishers.
36. J. Shackelford and W. Alexander, *CRC Materials Science and Engineering Handbook*. 3rd ed. 2000: CRC Press.
37. W. Chu, M. Mehregany, and R. Mullen, "Analysis of tip deflection and force of a bimetallic cantilever microactuator". *J. Micromech. Microeng.*, 3: p. 4-7. 1993.
38. K. Lai, *Thesis in Progress*, at *Electrical and Computer Engineering*. University of Manitoba: Winnipeg. 2005
39. J.D. Brazzle, M.R. Dokmeci, and C.H. Mastrangelo. "Modeling and characterization of sacrificial polysilicon etching using vapor-phase xenon difluoride" in *17th IEEE International Conference on Microelectromechanical Systems*. 2004.
40. D. Read and J. Dally, *Mechanics and Materials for Electronic Packaging: Thermal and Mechanical Behavior and Modeling*, ed. S. N. Vol. 2. 1994. 187.
41. H. Domer and O. Bostanjoglo, "Laser Ablation of thin films with very high induced stresses". *Journal of Applied Physics*, 91(8): p. 5462-5467. 2002.
42. R. Johnstone and M. Parameswaran. "Self-assembly of surface-micromachined structures using electrostatic attraction" in *SPIE MOEMS and Miniturized Systems II*. 2001.

APPENDICIES

APPENDIX A. Flowchart of XeF_2 Quick Pulse Etching

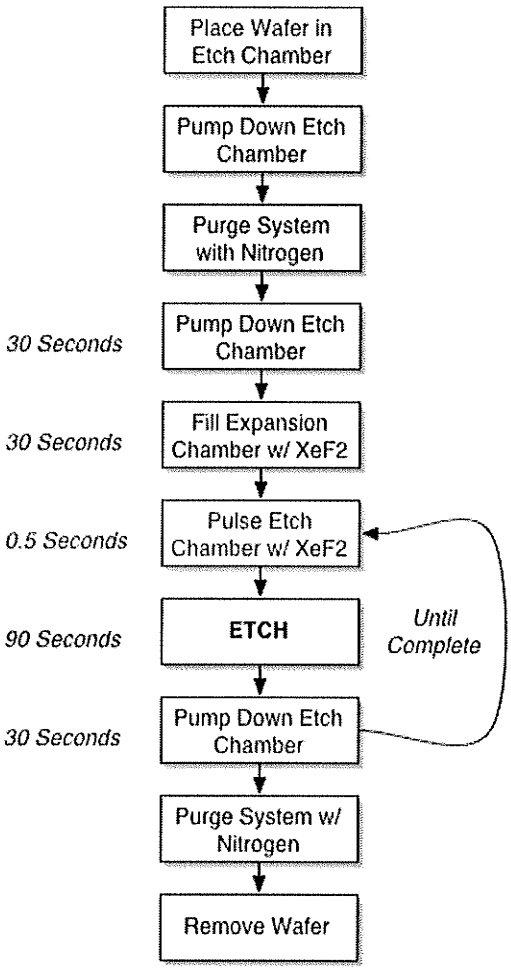

Figure A.1 XeF_2 Quick Pulse Etching Flowchart

APPENDIX B. Mask Layouts

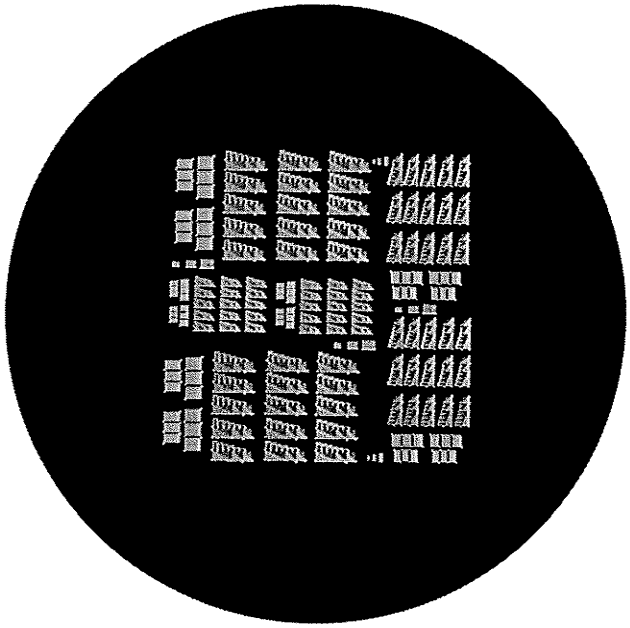

Figure B-1. Initial Stressed Magnetic Microactuator Wafer

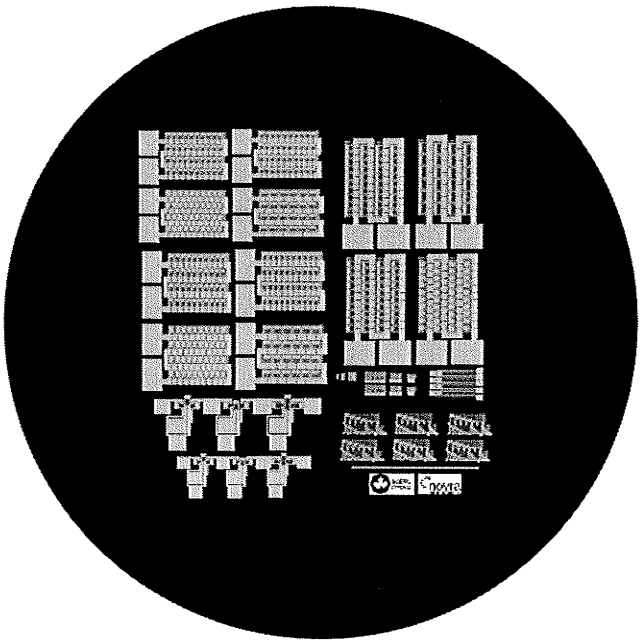

Figure B-2. Micro-reflector array and Self-Assembly wafer

APPENDIX C. SELF ASSEMBLY

Self-assembly was also attempted to show the versatility of the out-of-plane stressed magnetic microactuator and observe device interactions.

C.1 Self Assembly MEMS

Fabrication technology for micromachining devices typically limits the structures to be in plane with the wafer surface. Constructing fully three-dimensional (3-D) structures requires either depositing thicker films or assembling a two-dimensional (2-D) structure after its been released. Depositing thicker films has several disadvantages including limitations in fabrication and design. Some physical deposition processes such as thermal evaporation cannot achieve thick films without using several charges that typically requires reloading the evaporating system. Design limitations of using a thick film include the inability to pattern the sidewalls and limited use of angles in construction. Post-fabrication assembly of MEMS devices typically occurs after the release of the elements of the 3-D structure. The final structure can be assembled manually by a skilled operator, or by self-assembly. Manual assembly is typically time consuming, and cannot be done in a parallel fashion as can be done with self-assembly. Self-assembly of MEMS devices typically refers to applying a stimulus to position an actuator in a position where it may be locked or held by another actuated structure. In many cases this is achieved by using hinged and slotted MEMS structures.

An example of self-assembly implemented using electrostatic attraction as a form of stimulus was done in [42]. A voltage bias was applied between the released hinged structure and a conducting plate parallel to wafer surface. The strength of the electric field must be large enough to overcome gravitational forces to lift the structures into place. This form of self-assembly can be performed with biases as low as 35 volts. The hinged mirrors were constructed with a Multi-User MEMS process (MUMPs) called Cronos developed by JDS Uniphase.

Plastic deformation magnetic assembly (PDMA) is another form of self-assembly for MEMS structures. This technique was demonstrated in [34] by using plastic deformation of cantilever beams in order for the structures to hold their positions (see Figure C-1). The cantilever beams (or flaps) are electroplated with a magnetic Permalloy (NiFe) to allow for magnetic actuation. Bending occurs when an external magnetic field is applied to the wafer surface. The structure is able to bend to a maximum bending angle (θ), which is a function of parameters such as beam length and Permalloy volume. The structure then releases to a certain resting angle (ϕ) due to mechanical restoring forces that is typically

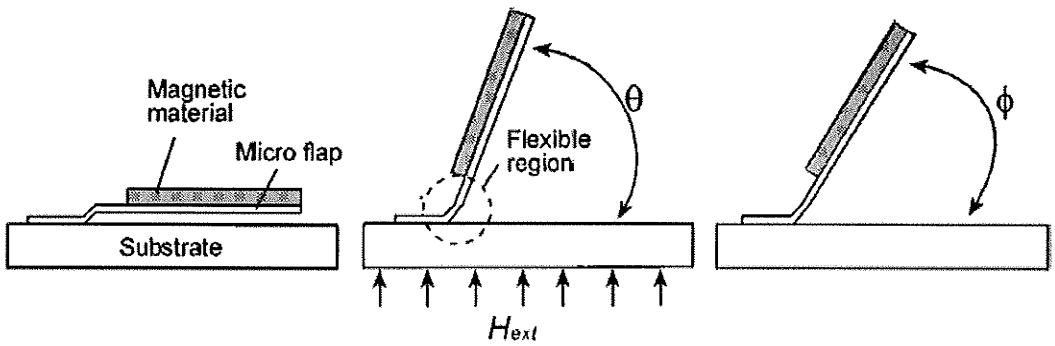

Figure C-1. Plastic Deformation Magnetic Assembly schematic [34]

smaller than the maximum bending angle. The difference between the maximum bending angle and resting angle is dependant on the stress characteristics of the bending material. Figure C-1 shows a schematic of the magnetic assembly system including the location of the Permalloy and the bending (flexible) region.

C.2 Design of Magnetic Self-Assembly Actuators

In this thesis, several stressed magnetic microactuators were configured in a manner in which post-fabrication assembly may be possible. The design that has shown success with previous experiments is perturbed by the addition of a "forked" structure at the tip of the actuator. This is to provide a latching mechanism for the self-assembly. An example of one of the configurations attempted can be seen in Figure C-2.

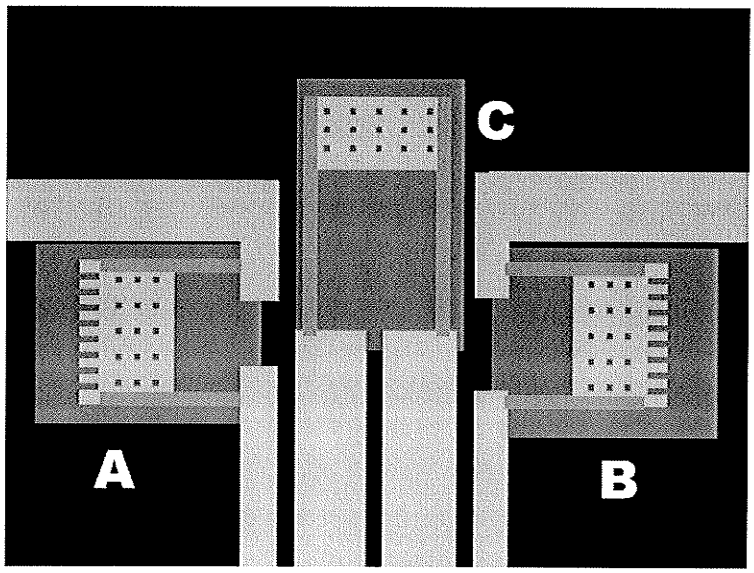

Figure C-2. Schematic of magnetic self-assembly actuators

In Figure C-2, actuators A and B are positioned so that they may latch on to actuator C. All the actuators are connected to a common ground, however may be actuated independently. Dimensions were varied in order to permit latching at the sides of the structure, as well as at the bottom of the reflector. Actuators A and B may be positioned by applying sufficient magnetic force to plastically deform the actuators greater than 90 degrees from their initial position.

C.3 Magnetic Self-Assembly Results

Self-assembly actuators were fabricated in parallel with the micro-reflector array since the fabrication process is identical. Six different designs were attempted, however due to their location on the wafer surface only two sets of actuators successfully released when actuated. Both sets performed in a similar manner and therefore the discussion of results will be grouped together.

Actuator C is initially positioned to prevent the forked actuators (A,B) from making contact when they are excessively actuated. The forked actuators are connected in series to provide similar displacement when driven with a current. A large current is applied (90mA) to the actuators to plastically deform the actuators so that their rest angle was greater than 90 degrees. Due to inconsistent underetching, the actuators did not move in a similar fashion (Figure C-3). The forked actuators are then separated slightly to allow actuator C to be positioned and latched between the

forked actuators. When the applied current is removed from the forked actuators, the restoring forces cause the structures to move inward to latch actuator C.

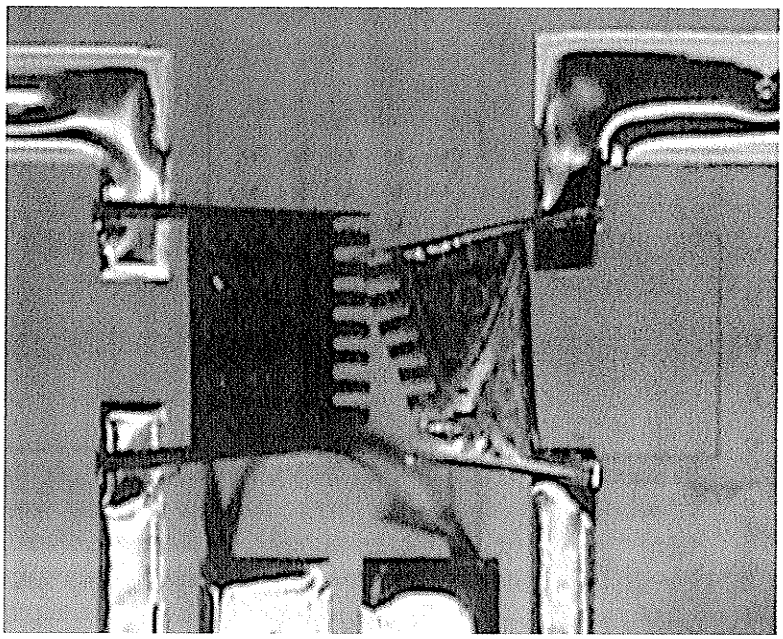

Figure C-3 Dissimilar actuation of magnetic self-assembly structures

Due to the curvature of the structure at the flexures and the geometry forked structure did not permit latching (Figure C-4). The insufficient finger spacing and poor fork location are the major problems with this particular design. When two actuators come in contact with each other, there does not appear to be any adverse effects. This implies that electrical contact between the actuators is poor relative to that of the connected structure. If an electrical path is formed through the interaction of two actuators, the reduction in current may also cause the actuators to disengage.

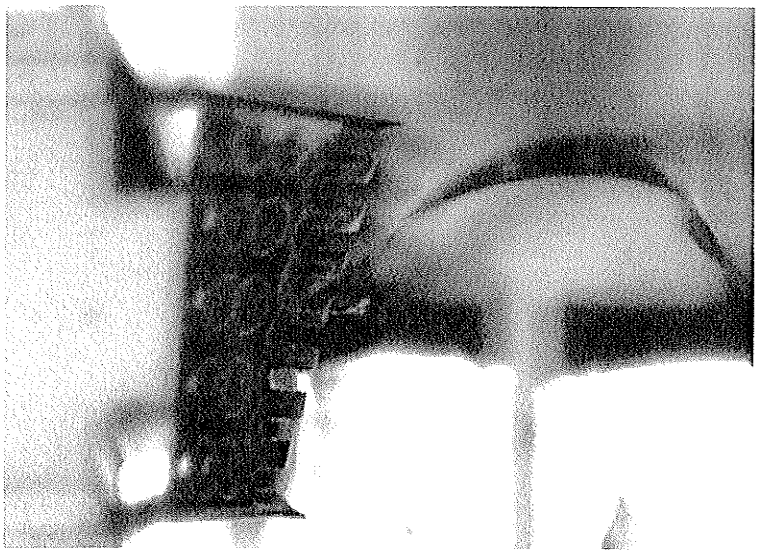

Figure C-4. Poor latching of stressed magnetic actuators

Future designs may implement the same conceptual design and layout, however should incorporate the latching fingers on the sides of actuator rather than on the top. Finger spacing should also be increased to no less than the width of the flexures. Increasing the aluminum/chrome thickness ratio may reduce the severity of the curvature seen on the initial fabrication.

APPENDIX D. MATLAB Plot code

```
% micro-mirror modeling
% jeremy Johnson
% micromirror.m

% init
clc
clear all
close all

% Aluminum Properties
t_al=0.5e-6;      % thickness
fw_al=56e-6*2;    % flexure width (two flexures)
fw10_al=70e-6*2;  % flexure width (scaled) (two flexures)
W5_al=600e-6;     % device width
W6_al=1200e-6;    % device width
W10_al=800e-6;    % device width (scaled)
h_reflect=300e-6; % reflector height
E_al=70e9;        % youngs modulus
a_al=25e-6;       % alpha(1/K)
d_al=2700;        % density of aluminum (kg/m^3)
p_alum=26e-9;     % resisitivty of aluminum
k_alum=237;       % thermal conductivity of Al (W/mC)
sig_al=124e6;     % Yield Strength of Aluminum
L=800e-6;         % flexure length
L10=1000e-6;      % flexure length (scaled)

% Chrome Properties
t_cr=0.1e-6;      % thickness
fw_cr=25e-6;      % flexure width
E_cr=140e9;       % youngs modulus
sig_cr=1000e6;    % yield strength
a_cr=6e-6;        % alpha (1/K)
d_cr=7190;        % density of aluminum

% other variables
B=0.25;           % magnetic field (Teslas)
bendLength=40e-6;  % bending length
interval=0.0001;          % current step resolution
I=0:interval:0.03;        % current interval

% Measured Data
%---------------
current=0:2.5e-3:25e-3;
current10=0:2e-3:24e-3;
set5= [69.33 72.19 74.65 78.46 82.56 85.28 90 93.37 97.44 101.54 105.35];
set6= [90 101.12 110.86 120.29 127.46 133.03 137.88 141.84 146.18 149.36 152.89];
set10=[79.76 84.90 87.45 90 93.557 96.38 100.24 102.84 105.47 108.13 112.47 117.53 122.23];

% combined material/weighted averages
t=t_al+t_cr;                                    % total thickness
E=E_al*(t_al/(t_al+t_cr))+E_cr*(t_cr/(t_al+t_cr));     % weighted average of youngs modulus
sig=sig_al*(t_al/(t_al+t_cr))+sig_cr*(t_cr/(t_al+t_cr));% weighted average of yield strength


% moment of inertia
in=fw_al*t^3/12;          % inertia of beam
```

```
in10=fw10_al*t^3/12;      % inertia of scaled beam


% simulated deflection angle

% initial positions
theta5B=set5(1);
theta6B=set6(1);
theta10B=set10(1);

for x=2:length(I)
    % Compute Scaling Factor of force based on previous angle
    factor5=sin(theta5B(x-1)*3.14159/180);
    factor6=sin(theta6B(x-1)*3.14159/180);
    factor10=sin(theta10B(x-1)*3.14159/180);

    % Calculate New Position
    theta5B(x)= ((interval*W5_al*B*L*bendLength/(E*in))*180/3.14159)*factor5+theta5B(x-1);
    theta6B(x)= ((interval*W6_al*B*L*bendLength/(E*in))*180/3.14159)*factor6+theta6B(x-1);
    theta10B(x)=
((interval*W10_al*B*L10*bendLength/(E*in10))*180/3.14159)*factor10+theta10B(x-1);
end

% measured data

figure
plot (current,set5,'x',current,set6,'o',current10,set10,'d')
legend('800x600um Micro-mirror Measured','800x1200um Micro-mirror Measured', '1000x800um
Micro-mirror Measured')
xlabel('Current (A)','FontSize',14)
ylabel('Angular Deflection (degrees)','FontSize',14)


% measured data w/ simulated data

figure
plot (current,set5,'x',current,set6,'o',current10,set10,'d',I,theta5B,'-',I,theta6B,I,theta10B)
legend('800x600um Micro-mirror Measured','800x1200um Micro-mirror Measured', '1000x800um
Micro-mirror Measured','800x600um Micro-mirror Modelled','800x1200um Micro-mirror
Modelled','1000x800um Micro-mirror Modelled')
xlabel('Current (A)','FontSize',14)
ylabel('Angular Deflection (degrees)','FontSize',14)


% elastic to plastic transition
e2p_theta = (sig*fw_al*t^2*bendLength/(4*E*in))*180/pi

% basic cantilever equation
F= max(I)*W5_al*B*sin(set5(1)); % force
d= F*L^3/(3*E*in);          % deflection distance
bTheta = (d/L)*(180/pi)     % deflection angle

% Thermal/Electrical/Magnetic Comparison

% other constants
perm_fSpace = 8.854e-12;
```

```
eval_angle=0:0.001:1;
current=0.100;
resist=1;
To=0;          % Initial Temperature
Tf=0.1:0.1:50;  % Final Temperature


% electrostatic force
l_midrefl=L-h_reflect/2                    % distance to middle of reflector
d_reflect=sin(eval_angle*pi/180)*650e-6          % reflector/substrate seperation
V=50e-3;                                % approximate voltage
F_ele=(perm_fSpace*h_reflect*fw_al*V^2)./(2*d_reflect.^2)   % approximate electrostatic force

% magnetic force
F_mag=current*fw_al*B*sin(eval_angle*pi/180)

%  electrostatic/magnetic comparison
figure
semilogy(eval_angle,F_ele,'--',eval_angle,F_mag,'-')
xlabel ('Angle (degrees)')
ylabel ('Force (N)')
legend ('Electrostatic','Magnetic')

% thermal
fw_al=112e-6;      % since 2 flexure arms, width effectively doubled
b_cr=112e-6;

R =
((fw_al*E_al*t_al^2)^2+(b_cr*E_cr*t_cr^2)^2+2*fw_al*b_cr*E_al*E_cr*t_al*t_cr*(2*t_al^2+3*t_al*t
_cr+2*t_cr^2))./(6*fw_al*b_cr*E_al*E_cr*t_al*t_cr*(t_al+t_cr)*(a_al-a_cr)*(Tf-To));
dThermal =(1./R)*L^2/2;        % thermal displacement
in=fw_al*t^3/12;               % inertia of beam
F_therm=3*E*in*dThermal/L^3     % thermal force

current=sqrt(2*(Tf*k_alum*(fw_al*t_al)^2)/(L^2*p_alum));   % current at given temp
F_mag2=current*W5_al*B*sin(5*pi/180)
F_mag3=current*W5_al*B*sin(45*pi/180)
F_mag4=current*W5_al*B*sin(90*pi/180)
figure
plot (current, F_therm,'-',current, F_mag2,'--',current, F_mag3,'-.',current, F_mag4, ':')
xlabel ('Current (A)')
ylabel ('Force (N)')
legend ('Thermal','Magnetic @ 5 degrees', 'Magnetic @ 45 degrees', 'Magnetic @ 90 degrees')


% Comparing Thermal Sims to Actual

fw_al=112e-6;      % since 2 flexure arms, width effectively doubled
b_cr=112e-6;
To=0;              % Initial Temperature
Tf=0.1:0.1:70;     % Final Temperature
current=sqrt(2*(Tf*k_alum*(fw_al*t_al)^2)/(L^2*p_alum));   % current at given temp

R =
((fw_al*E_al*t_al^2)^2+(b_cr*E_cr*t_cr^2)^2+2*fw_al*b_cr*E_al*E_cr*t_al*t_cr*(2*t_al^2+3*t_al*t
_cr+2*t_cr^2))./(6*fw_al*b_cr*E_al*E_cr*t_al*t_cr*(t_al+t_cr)*(a_al-a_cr)*(Tf-To));
dThermal =(1./R)*L^2/2;        % thermal displacement
I=fw_al*t^3/12;                % inertia of beam
```

```
F_therm=3*E*I*dThermal/L^3      % thermal force
T = F_therm * L ;               % Torque F*d
Lm = 40e-6;                     % observed bending length
theta=Lm*T/(E*I);               % theta (rad)
thetaDeg = theta * 180/pi;      % theta (deg)

figure
plot (current,thetaDeg)
xlabel ('Current (A)')
ylabel ('Angle (Degrees)')
```